

DETERMINATION OF A TRANSVERSELY ISOTROPIC MEDIUM EQUIVALENT TO A FRACTURED FLUID-SATURATED POROELASTIC MEDIUM. A FINITE ELEMENT APPROACH*

JUAN E. SANTOS[†], ROBIEL MARTÍNEZ CORREDOR[‡], AND JOSÉ M. CARCIONE[§]

Abstract. The purpose of this work is to present a numerical upscaling procedure to determine a viscoelastic material equivalent to a horizontally fractured fluid-saturated poroelastic—Biot—medium where fractures are modeled as explicit boundary conditions. At long wavelengths compared to the average distance between fractures, the Biot medium behaves as an equivalent (effective) transversely isotropic and viscoelastic (TIV) medium. The stiffness components of the TIV medium are determined using a finite element (FE) technique based on time-harmonic experiments. Each experiment is associated with a boundary value problem (BVP) representing compressibility and shear experiments applied to a sample of the fractured Biot medium. The solutions of these BVP allow us to measure the changes in volume and shape of the sample which in turn determine the stiffness components. Uniqueness of the solution of the continuous and discrete BVP's is demonstrated and a priori L^2 and H^1 error estimates are derived. The procedure to determine the stiffness components is validated against a theory valid for uniform media, fluid flow perpendicular to the fracture layering, and independent of the loading direction. Finally, an example for the case of patchy gas-brine saturation for which no analytical solution is available is presented.

Key words. poroelasticity, fractures, boundary conditions, finite element methods and effective anisotropic media

AMS subject classifications. 65Z05, 8602, 8608

DOI. 10.1137/15M1040876

1. Introduction. Reservoir rocks have in many cases plane compliant discontinuities, like fractures and faults, that in general control the hydrocarbon flow and production in the reservoir [1], [2]. Also, in many cases reservoirs rocks contain dense sets of fractures aligned in preferred directions.

Numerical simulations of seismic wave propagation through fractured reservoirs require an interface model describing the seismic response of fractures. A fracture embedded in a fluid-saturated poroelastic—Biot—medium is a very thin compliant and highly permeable layer. Since the layer thickness is on the order of millimeters, much smaller than the predominant wavelengths of the traveling waves, any finite difference (FD) or finite element (FE) spatial discretization of a fractured reservoir would require extremely fine meshes to simulate wave propagation in the reservoir, making the procedure unfeasible. Thus, numerical simulations of seismic wave propagation through fractured reservoirs requires an interface model describing the seismic response of fractures.

*Submitted to the journal's Computational Methods in Science and Engineering section September 22, 2015; accepted for publication (in revised form) December 2, 2016; published electronically March 9, 2017.

<http://www.siam.org/journals/sisc/39-2/M104087.html>

Funding: This work was supported by CONICET under grant 112-2011010-0777.

[†]Instituto del Gas y del Petróleo, Facultad de Ingeniería, Universidad de Buenos Aires, CONICET, Av. Las Heras 2214 Piso 3 C1127AAR Buenos Aires, Argentina, and Universidad Nacional de La Plata, La Plata, Provincia de Buenos Aires, Argentina, and Department of Mathematics, Purdue University, West Lafayette, IN, 47907-2067 (santos@math.purdue.edu).

[‡]Facultad de Ingeniería, Universidad Nacional de La Plata, Calle 1 y 47, La Plata (B1900TAG), Provincia de Buenos Aires, Argentina (martinezcorredor@gmail.com).

[§]Istituto Nazionale di Oceanografia e di Geofisica Sperimentale (OGS), Borgo Grotta Gigante 42c, 34010 Sgonico, Trieste, Italy (jcarcione@inogs.it).

In this paper, fractures are modeled using a set of boundary conditions proposed by Nakagawa and Schoenberg [3] to represent fluid-solid interaction within a fracture and the effect of its permeability on seismic wave scattering. These boundary conditions impose continuity of the total stress components, pressure discontinuities proportional to average fluid velocities across the fracture, and displacement discontinuities proportional to stress components and average fluid pressures along the fracture.

This interface model allows us to represent wave-induced fluid flow, by which the fast waves are converted to slow (diffusive) Biot waves when traveling across fractures (mesoscopic-loss) heterogeneities [4], [5].

In [6], White, Mikhaylova, and Lyakhovitskiy were the first to introduce the mesoscopic-loss mechanism using the Biot theory considering alternating thin poroelastic layers along the direction perpendicular to the layering plane [4].

A dense set of horizontal fractures in a fluid-saturated poroelastic medium behaves as a TIV medium when the average fracture distance is much smaller than the predominant wavelength of the traveling waves. This leads to frequency and angular variations of velocity and attenuation of seismic waves.

Gelinsky and Shapiro [7] obtained the relaxed and unrelaxed stiffnesses of the equivalent poroviscoelastic medium to a finely layered horizontally homogeneous material. Krzikalla and Müller [8] combined the two previous models to obtain the five complex and frequency-dependent stiffnesses of the equivalent transversely isotropic viscoelastic (TIV) medium. Their approach assumes that the fluid-flow direction is perpendicular to the fracture layering. The model considers only one relaxation function, corresponding to the symmetry-axis compressional wave stiffness. These assumptions fail for heterogeneous layers, where the propagation of waves may depend on direction.

FE harmonic compressibility and shear tests are first presented in [9] to obtain a viscoelastic medium-long wavelength equivalent to a highly heterogeneous isotropic sample. Then, in [10], [11], and [12] the procedure is extended to determine long-wave equivalent media to finely layered viscoelastic and poroelastic materials.

The novel aspects of this work reside in the fact that the procedure presented here can be used to study the wave-propagation characteristics of fluid-saturated poroelastic fractured media with arbitrary (heterogeneous) properties of the background medium and fractures. This can be performed only by using a numerical method such as the FEM method. In addition, we obtain the stress-strain relation through the complex stiffness components. To the best of our knowledge, no other similar technique has been proposed for porous media, where fractures have been modeled explicitly as boundary conditions.

Among other authors employing numerical simulations to study attenuation and dispersion effects in fluid-saturated poroelastic materials, we mention Saenger et al. [13] where they present numerical simulations in two-dimensional (2D) and three-dimensional (3D) media porous media saturated with fluids to analyze Biot's predictions in the high and low frequency limits of poroelasticity. Also, numerical approaches to determine effective media corresponding to fractured rocks were presented by Grechka and Kachanov [14], [15], where they perform 3D static finite-element simulations, summing up the individual contributions of the fractures and ignoring their interactions.

In this work, we present and analyze a collection of time-harmonic FE compressibility and shear experiments on fluid-saturated poroelastic samples with an embedded dense set of horizontal fractures represented as internal boundary conditions within

the sample.

Each experiment is associated with a boundary value problem (BVP) representing compressibility and shear tests, allowing us to determine the complex and frequency dependent stiffnesses of the effective TIV medium at the macroscale. Thus this procedure can be regarded as a numerical upscaling method to bring the effect of the mesoscale fractures to the macroscale.

To discretize each component of the solid displacement vector, we employ locally piecewise bilinear functions that are discontinuous along the fractures. For the fluid phase we use locally the vector part of the Raviart–Thomas–Nedelec space of zero order [16], also making them discontinuous along fractures.

First, we derived a variational formulation of the continuous problems and analyzed their uniqueness. Then, we formulated the FE procedures and derived a priori L^2 and H^1 estimates which are optimal for the given regularity of the solution.

Next, the a priori L^2 error estimate is computationally confirmed by carrying out mesh refinements, while the quasistatic experiments to determine the stiffnesses coefficients are validated by comparison with the theory by Krzikalla and Müller [8]. Finally, the methodology is applied to the case of patchy gas-brine saturation, for which no analytical solutions are available.

2. A Biot medium. The modeling method at the mesoscale. This section presents the stress-strain relations and Biot’s equation in the diffusive range as well as the boundary conditions to model fractures embedded in a poroelastic solid saturated by a single-phase compressible viscous fluid (a Biot medium). All equations will be stated in the space-frequency domain. Biot’s equations will be solved on a representative sample of the fractured material with appropriate boundary conditions associated with compressibility and shear harmonic experiments. The FE solutions will allow us to measure volume and shape changes in the sample that in turn will allow us to determine the stiffness coefficients of the equivalent TIV medium at the macroscale.

2.1. The stress-strain relations in a Biot medium. We consider a fractured Biot medium and assume that the whole aggregate is isotropic. Let the superindex (θ) , $\theta = b, f$ indicate solid matrix and saturant fluid properties associated with the background and fractures, respectively.

Let $\mathbf{u}_s = (u_{s,i})$ and $\tilde{\mathbf{u}}_f = (\tilde{u}_{f,i})$, $i = 1, \dots, 3$, denote the averaged displacement vectors of the solid and fluid phases, respectively. Also let

$$\mathbf{u}_f = \phi^{(\theta)}(\tilde{\mathbf{u}}_f - \mathbf{u}_s)$$

be the average relative fluid displacement per unit volume of bulk material, with $\phi^{(\theta)}$ denoting the effective porosity. Set $\mathbf{u} = (\mathbf{u}_s, \mathbf{u}_f)$ and note that

$$\xi = -\nabla \cdot \mathbf{u}_f$$

represents the change in fluid content.

Let $\boldsymbol{\varepsilon}(\mathbf{u}_s)$ be the linearized strain tensor of the solid. Also, let $\boldsymbol{\tau}$ and p_f denote the stress tensor of the bulk material and the fluid pressure, respectively.

Following [17], the linear stress-strain relations in our fractured fluid-saturated poroelastic medium are

$$(1a) \quad \tau_{st}(\mathbf{u}) = 2G^{(\theta)} \boldsymbol{\varepsilon}_{st}(\mathbf{u}_s) + \delta_{st}(\lambda_U^{(\theta)} \nabla \cdot \mathbf{u}_s - \alpha^{(\theta)} M^{(\theta)} \xi),$$

$$(1b) \quad p_f(\mathbf{u}) = -\alpha^{(\theta)} M^{(\theta)} \nabla \cdot \mathbf{u}_s + M^{(\theta)} \xi, \quad \theta = b, f.$$

In (1a) δ_{st} denotes the Kroenecker delta. Also, the coefficient $G^{(\theta)}$ is equal to the shear modulus of the bulk material, considered to be equal to the shear modulus of the dry matrix. Besides

$$(2) \quad \lambda_U^{(\theta)} = K_U^{(\theta)} - \frac{2}{3}G^{(\theta)},$$

with $K_U^{(\theta)}$ being the bulk modulus of the saturated material. Following [18] and [19], the coefficients in (1a)–(1b) can be obtained from the relations

$$(3) \quad \alpha^{(\theta)} = 1 - \frac{K_m^{(\theta)}}{K_s^{(\theta)}}, \quad M^{(\theta)} = \left(\frac{\alpha^{(\theta)} - \phi^{(\theta)}}{K_s^{(\theta)}} + \frac{\phi^{(\theta)}}{K_f^{(\theta)}} \right)^{-1},$$

$$K_U^{(\theta)} = K_m^{(\theta)} + (\alpha^{(\theta)})^2 M^{(\theta)}, \quad \theta = b, f,$$

where $K_s^{(\theta)}$, $K_m^{(\theta)}$, and $K_f^{(\theta)}$ denote the bulk modulus of the solid grains composing the solid matrix, the dry matrix, and the saturant fluid, respectively. The coefficient $\alpha^{(\theta)}$ is known as the effective stress coefficient of the bulk material.

2.2. The boundary conditions at a fracture inside a Biot medium. Consider a rectangular domain $\Omega = (0, L_1) \times (0, L_3)$ with boundary Γ in the (x_1, x_3) -plane, with x_1 and x_3 being the horizontal and vertical coordinates, respectively.

Let us assume that the domain Ω contains a set of $J^{(f)}$ horizontal fractures $\Gamma^{(f,l)}$, $l = 1, \dots, J^{(f)}$ each one of length L_1 and aperture $h^{(f)}$. This set of fractures divides Ω in a collection of nonoverlapping rectangles $R^{(l)}$, $l = 1, \dots, J^f + 1$, so that

$$\Omega = \cup_{l=1}^{J^{(f)}+1} R^{(l)}.$$

Figure 1 shows a prototype model of the fractured sample Ω .

Consider a fracture $\Gamma^{(f,l)}$ and the two rectangles $R^{(l)}$ and $R^{(l+1)}$ having as a common side $\Gamma^{(f,l)}$. Let $\nu_{l,l+1}$ and $\chi_{l,l+1}$ be the unit outer normal and a unit tangent (oriented counterclockwise) on $\Gamma^{(f,l)}$ from $R^{(l)}$ to $R^{(l+1)}$, such that $\{\nu_{l,l+1}, \chi_{l,l+1}\}$ is an orthonormal system on $\Gamma^{(f,l)}$.

Let $[\mathbf{u}_s], [\mathbf{u}_f]$ denote the jumps of the solid and fluid displacement vectors at $\Gamma^{(f,l)}$, i.e.,

$$[\mathbf{u}_s] = \left(\mathbf{u}_s^{(l+1)} - \mathbf{u}_s^{(l)} \right) |_{\Gamma^{(f,l)}},$$

where $\mathbf{u}_s^{(l)} \equiv \mathbf{u}_s|_{R^{(l)}}$ denotes the trace of \mathbf{u}_s as seen from to $R^{(l)}$.

The following boundary conditions on $\Gamma^{(f,l)}$, representing the approximate acoustic response of a fracture as a very thin, compliant, and highly permeable layer, are derived in [3, eq. (52)]:

$$(4) \quad [\mathbf{u}_s \cdot \boldsymbol{\nu}_{l,l+1}] = \eta_N \left((1 - \alpha^{(f)} \tilde{B}^{(f)} (1 - \Pi)) \boldsymbol{\tau}(\mathbf{u}) \boldsymbol{\nu}_{l,l+1} \cdot \boldsymbol{\nu}_{l,l+1} - \alpha^{(f)} \frac{1}{2} \left((-p_f^{(l+1)}) + (-p_f^{(l)}) \right) \Pi \right), \quad \Gamma^{(f,l)},$$

$$(5) \quad [\mathbf{u}_s \cdot \boldsymbol{\chi}_{l,l+1}] = \eta_T \boldsymbol{\tau}(\mathbf{u}) \boldsymbol{\nu}_{l,l+1} \cdot \boldsymbol{\chi}_{l,l+1}, \quad \Gamma^{(f,l)},$$

$$(6) \quad [\mathbf{u}_f \cdot \boldsymbol{\nu}_{l,l+1}] = \alpha^{(f)} \eta_N \left(-\boldsymbol{\tau}(\mathbf{u}) \boldsymbol{\nu}_{l,l+1} \cdot \boldsymbol{\nu}_{l,l+1} + \frac{1}{\tilde{B}^{(f)}} \frac{1}{2} \left((-p_f^{(l+1)}) + (-p_f^{(l)}) \right) \right) \Pi, \quad \Gamma^{(f,l)},$$

$$(7) \quad (-p_f^{(l+1)}) - (-p_f^{(l)}) = \frac{i\omega\mu^{(f)}\Pi}{\hat{\kappa}^{(f)}} \frac{1}{2} \left(\mathbf{u}_f^{(l+1)} + \mathbf{u}_f^{(l)} \right) \cdot \boldsymbol{\nu}_{l,l+1}, \quad \Gamma^{(f,l)},$$

$$(8) \quad \boldsymbol{\tau}(\mathbf{u}) \boldsymbol{\nu}_{l,l+1} \cdot \boldsymbol{\nu}_{l,l+1} = \boldsymbol{\tau}(\mathbf{u}) \boldsymbol{\nu}_{l+1,l} \cdot \boldsymbol{\nu}_{l+1,l}, \quad \Gamma^{(f,l)},$$

$$(9) \quad \boldsymbol{\tau}(\mathbf{u}) \boldsymbol{\nu}_{l,l+1} \cdot \boldsymbol{\chi}_{l,l+1} = \boldsymbol{\tau}(\mathbf{u}) \boldsymbol{\nu}_{l+1,l} \cdot \boldsymbol{\chi}_{l+1,l}, \quad \Gamma^{(f,l)}.$$

Here η_N and η_T are the normal and tangential fracture compliances, respectively. Also, $\mu^{(f)}$ is the fluid viscosity in the fracture and

$$(10) \quad \hat{\kappa}^{(f)} = \frac{\kappa^{(f)}}{h^{(f)}}.$$

The fracture dry plane wave modulus $H_m^{(f)} = K_m^{(f)} + \frac{4}{3}G^{(f)}$ and the dry fracture shear modulus $G^{(f)}$ are defined in terms of the fracture aperture $h^{(f)}$ and the fracture compliances by the relations

$$(11) \quad \eta_N = \frac{h^{(f)}}{H_m^{(f)}}, \quad \eta_T = \frac{h^{(f)}}{G^{(f)}}.$$

Besides,

$$(12) \quad \epsilon = \frac{(1+i)}{2} \left(\frac{\omega\mu^{(f)}\alpha^{(f)}\eta_N}{2\tilde{B}^{(f)}\hat{\kappa}^{(f)}} \right)^{1/2}, \quad \Pi(\epsilon) = \frac{\tanh \epsilon}{\epsilon}, \quad \tilde{B}^{(f)} = \frac{\alpha^{(f)}M^{(f)}}{H_U^{(f)}}.$$

Note that $\Pi = \text{Re}(\Pi) - i \text{Im}(\Pi) \equiv \Pi_R - i \Pi_I$ with $\Pi_R > 0, \Pi_I > 0$.

In the high-permeability limit ($\kappa \rightarrow \infty$), it can be seen that $\Pi \rightarrow 1$ and (4)–(9) reduce to [3, eq. (53)]:

$$(13) \quad [\mathbf{u}_s \cdot \boldsymbol{\nu}_{l,l+1}] = \eta_N \left(\boldsymbol{\tau}(\mathbf{u}) \boldsymbol{\nu}_{l,l+1} \cdot \boldsymbol{\nu}_{l,l+1} - \alpha^{(f)} (-p_f^{(l+1)}) \right), \quad \Gamma^{(f,l)},$$

$$(14) \quad [\mathbf{u}_s \cdot \boldsymbol{\chi}_{l,l+1}] = \eta_T \boldsymbol{\tau}(\mathbf{u}) \boldsymbol{\nu}_{l,l+1} \cdot \boldsymbol{\chi}_{l,l+1}, \quad \Gamma^{(f,l)},$$

$$(15) \quad [\mathbf{u}_f \cdot \boldsymbol{\nu}_{l,l+1}] = \alpha \eta_N \left(-\boldsymbol{\tau}(\mathbf{u}) \boldsymbol{\nu}_{l,l+1} \cdot \boldsymbol{\nu}_{l,l+1} + \frac{1}{\tilde{B}^{(f)}} (-p_f^{(l+1)}) \right), \quad \Gamma^{(f,l)},$$

$$(16) \quad (-p_f^{(l+1)}) = (-p_f^{(l)}), \quad \Gamma^{(f,l)},$$

$$(17) \quad \boldsymbol{\tau}(\mathbf{u}) \boldsymbol{\nu}_{l,l+1} \cdot \boldsymbol{\nu}_{l,l+1} = \boldsymbol{\tau}(\mathbf{u}) \boldsymbol{\nu}_{l+1,l} \cdot \boldsymbol{\nu}_{l+1,l}, \quad \Gamma^{(f,l)},$$

$$(18) \quad \boldsymbol{\tau}(\mathbf{u}) \boldsymbol{\nu}_{l,l+1} \cdot \boldsymbol{\chi}_{l,l+1} = \boldsymbol{\tau}(\mathbf{u}) \boldsymbol{\nu}_{l+1,l} \cdot \boldsymbol{\chi}_{l+1,l}, \quad \Gamma^{(f,l)}.$$

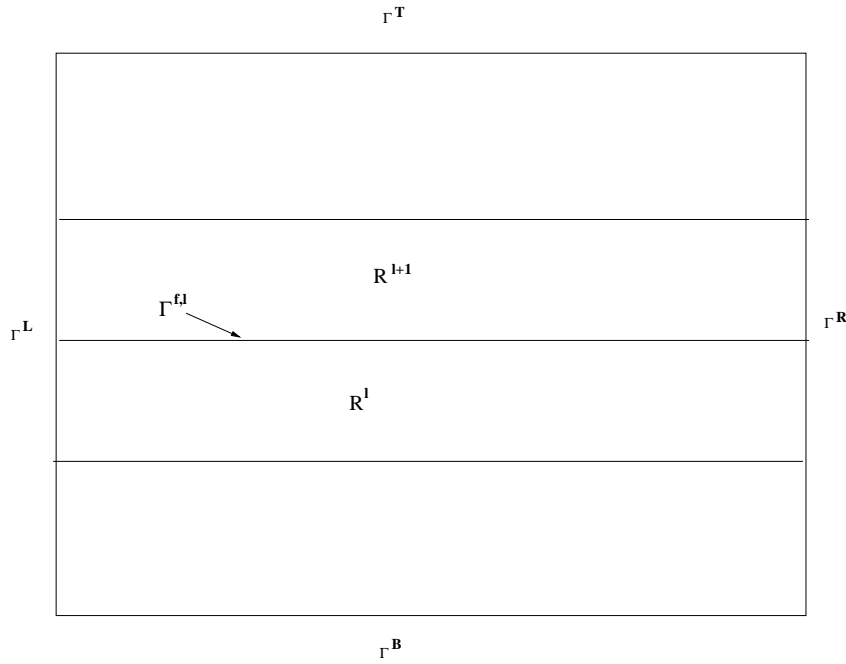


FIG. 1. Prototype model of the domain Ω with boundary $\Gamma = \Gamma^L \cup \Gamma^R \cup \Gamma^B \cup \Gamma^T$, the partition of Ω into rectangles $R^{(l)}$, and a horizontal fracture $\Gamma^{(f,l)}$ separating $R^{(l)}$ and $R^{(l+1)}$.

The analysis will be carried over for the more general fracture boundary conditions (4)–(9), with the analysis for the boundary conditions (13)–(18) being a particular case.

Set

$$(19) \quad a_{11} = \eta_N \left(1 - \alpha^{(f)} \tilde{B}^{(f)} (1 - \Pi) \right), \quad a_{12} = \alpha^{(f)} \eta_N \Pi,$$

$$a_{22} = \frac{\alpha^{(f)} \eta_N \Pi}{\tilde{B}^{(f)}}, \quad \Theta = a_{11} a_{22} - a_{12}^2.$$

Then from (4) and (6) we obtain

$$(20) \quad \boldsymbol{\tau}(\mathbf{u}) \boldsymbol{\nu}_{l,l+1} \cdot \boldsymbol{\nu}_{l,l+1} = \frac{a_{22}}{\Theta} [\mathbf{u}_s \cdot \boldsymbol{\nu}_{l,l+1}] + \frac{a_{12}}{\Theta} [\mathbf{u}_f \cdot \boldsymbol{\nu}_{l,l+1}], \quad \Gamma^{(f,l)},$$

$$(21) \quad (-p_f^{(l+1)}) + (-p_f^{(l)}) = 2 \frac{a_{12}}{\Theta} [\mathbf{u}_s \cdot \boldsymbol{\nu}_{l,l+1}] + 2 \frac{a_{11}}{\Theta} [\mathbf{u}_f \cdot \boldsymbol{\nu}_{l,l+1}], \quad \Gamma^{(f,l)}.$$

Adding (7) and (21),

$$(22) \quad (-p_f^{(l+1)}) = \frac{a_{12}}{\Theta} [\mathbf{u}_s \cdot \boldsymbol{\nu}_{l,l+1}] + \frac{a_{11}}{\Theta} [\mathbf{u}_f \cdot \boldsymbol{\nu}_{l,l+1}]$$

$$+ \frac{i\omega\mu^{(f)}\Pi}{\widehat{\kappa}^{(f)}} \frac{1}{4} \left(\mathbf{u}_f^{(l+1)} + \mathbf{u}_f^{(l)} \right) \cdot \boldsymbol{\nu}_{l,l+1}, \quad \Gamma^{(f,l)}.$$

Using (22) in (21), we get

$$(23) \quad (-p_f^{(l)}) = \frac{a_{12}}{\Theta} [\mathbf{u}_s \cdot \boldsymbol{\nu}_{l,l+1}] + \frac{a_{11}}{\Theta} [\mathbf{u}_f \cdot \boldsymbol{\nu}_{l,l+1}]$$

$$- \frac{i\omega\mu^{(f)}\Pi}{\widehat{\kappa}^{(f)}} \frac{1}{4} \left(\mathbf{u}_f^{(l+1)} + \mathbf{u}_f^{(l)} \right) \cdot \boldsymbol{\nu}_{l,l+1}, \quad \Gamma^{(f,l)}.$$

In the analysis that follows, we will employ the more convenient form of the boundary conditions given by (5), (8), (9), (20), (22), and (23).

2.3. Biot's equation in the diffusive range. Let the differential operator $\mathcal{L}(\mathbf{u})$ and the matrix $\mathbf{B} \in \mathbf{R}^{4 \times 4}$ be defined as

$$(24) \quad \mathcal{L}(\mathbf{u}) = (\nabla \cdot \boldsymbol{\tau}(\mathbf{u}), \nabla p_f(\mathbf{u})), \quad \mathbf{B} = \begin{pmatrix} 0I_2 & 0I_2 \\ 0I_2 & \frac{\mu^{(\theta)}}{\kappa^{(\theta)}} I_2 \end{pmatrix},$$

where I_2 is the 2×2 identity matrix, $\mu^{(\theta)}$ is the fluid viscosity, and $\kappa^{(\theta)}$ is the intrinsic permeability.

Biot's equations in the diffusive range and in the absence of external forces are [20], [21]:

$$(25) \quad i\omega \mathbf{B}\mathbf{u} + \mathcal{L}(\mathbf{u}) = 0,$$

where $i = \sqrt{-1}$ and ω is the angular frequency.

3. The macroscale. The equivalent TIV medium at long wavelengths.

At long wavelengths (or low frequencies) compared to the average distance between fractures and the size of the heterogeneities, the Biot medium behaves as an equivalent (effective) medium, whose stiffness components can be obtained by a FE technique based on oscillatory (harmonic) experiments over representative samples of the fractured material. Here, we illustrate this technique. In particular, there are analytical solutions that can be used to validate the numerical experiments.

As shown by Gelinsky and Shapiro [7], a horizontally fractured Biot medium behaves as a transversely isotropic (TI) medium with a vertical symmetry axis (the x_3 -axis) at long wavelengths. They obtained the low- and high-frequency limit real-valued stiffnesses, respectively. Later, assuming a one-dimensional (1D) character of the fluid pressure equilibration process, Krzikalla and Müller [8] presented a model to obtain the five complex and frequency-dependent stiffness p_{IJ} , $I, J = 1, \dots, 6$, of the equivalent TIV medium that is included in Appendix B.

Denote by $\sigma_{ij}(\tilde{\mathbf{u}}_s)$ and $\epsilon_{ij}(\tilde{\mathbf{u}}_s)$ the stress and strain tensor components of the equivalent TIV medium, where $\tilde{\mathbf{u}}_s$ denotes the solid displacement vector at the macroscale. The corresponding stress-strain relations, stated in the space-frequency domain, are [22], [5]

$$(26) \quad \sigma_{11}(\tilde{\mathbf{u}}_s) = p_{11} \epsilon_{11}(\tilde{\mathbf{u}}_s) + p_{12} \epsilon_{22}(\tilde{\mathbf{u}}_s) + p_{13} \epsilon_{33}(\tilde{\mathbf{u}}_s),$$

$$(27) \quad \sigma_{22}(\tilde{\mathbf{u}}_s) = p_{12} \epsilon_{11}(\tilde{\mathbf{u}}_s) + p_{11} \epsilon_{22}(\tilde{\mathbf{u}}_s) + p_{13} \epsilon_{33}(\tilde{\mathbf{u}}_s),$$

$$(28) \quad \sigma_{33}(\tilde{\mathbf{u}}_s) = p_{13} \epsilon_{11}(\tilde{\mathbf{u}}_s) + p_{13} \epsilon_{22}(\tilde{\mathbf{u}}_s) + p_{33} \epsilon_{33}(\tilde{\mathbf{u}}_s),$$

$$(29) \quad \sigma_{23}(\tilde{\mathbf{u}}_s) = 2 p_{55} \epsilon_{23}(\tilde{\mathbf{u}}_s),$$

$$(30) \quad \sigma_{13}(\tilde{\mathbf{u}}_s) = 2 p_{55} \epsilon_{13}(\tilde{\mathbf{u}}_s),$$

$$(31) \quad \sigma_{12}(\tilde{\mathbf{u}}_s) = 2 p_{66} \epsilon_{12}(\tilde{\mathbf{u}}_s).$$

In (26)–(31) we have assumed a closed system, for which the variation of fluid content $\zeta = -\nabla \cdot \mathbf{u}_f$ is equal to zero. The p_{IJ} are the complex and frequency-dependent Voigt stiffnesses to be determined using the solution of the harmonic experiments.

Note that in a TIV medium the following relation holds [5]:

$$(32) \quad p_{12} = p_{11} - 2 p_{66}$$

so that only five independent stiffness coefficients need to be considered.

In the next sections we present and analyze a FE procedure to determine the coefficients in equations (26)–(31) and the corresponding velocities and quality factors. These properties, which depend on frequency and propagation direction, are given in Appendix C.

To determine each stiffness p_{IJ} we will solve Biot’s equation (25) together with the fracture boundary conditions (5), (8), (9), (20), (22), and (23) and additional boundary conditions to be defined in the next section.

4. The quasistatic experiments to determine the stiffnesses p_{IJ} . Here we show that the stiffness p_{IJ} can be determined applying a set of compressibility and shear tests on a 2D representative sample $\Omega = (0, L_1) \times (0, L_3)$ of boundary $\Gamma = \partial\Omega$ of the fractured Biot material in the (x_1, x_3) -plane. Each test is defined as a BVP in the space-frequency domain which will be solved using a FE procedure. The solutions of each test will allow us to measure volume and shape changes in the sample Ω . Below it is explained how those changes determine in turn the stiffnesses p_{IJ} .

Set $\Gamma = \Gamma^L \cup \Gamma^B \cup \Gamma^R \cup \Gamma^T$, where

$$\begin{aligned} \Gamma^L &= \{(x_1, x_3) \in \Gamma : x_1 = 0\}, & \Gamma^R &= \{(x_1, x_3) \in \Gamma : x_1 = L_1\}, \\ \Gamma^B &= \{(x_1, x_3) \in \Gamma : x_3 = 0\}, & \Gamma^T &= \{(x_1, x_3) \in \Gamma : x_3 = L_3\}. \end{aligned}$$

Denote by ν the unit outer normal on Γ , and let χ be a unit tangent on Γ so that $\{\nu, \chi\}$ is an orthonormal system on Γ .

4.1. Determination of p_{33} . Consider the solution of (25) in Ω with the fracture boundary conditions (5), (8), (9), (20), (22), and (23) together with the following boundary conditions:

$$(33) \quad \tau(\mathbf{u})\nu \cdot \nu = -\Delta P, \quad (x_1, x_3) \in \Gamma^T,$$

$$(34) \quad \tau(\mathbf{u})\nu \cdot \chi = 0, \quad (x_1, x_3) \in \Gamma,$$

$$(35) \quad \mathbf{u}_s \cdot \nu = 0, \quad (x_1, x_3) \in \Gamma \setminus \Gamma^T,$$

$$(36) \quad \mathbf{u}_f \cdot \nu = 0, \quad (x_1, x_3) \in \Gamma.$$

Denoting by V the original volume of the sample, its (complex) oscillatory volume change, $\Delta V(\omega)$, allows us to define p_{33} by using the relation

$$(37) \quad \frac{\Delta V(\omega)}{V} = -\frac{\Delta P}{p_{33}(\omega)},$$

valid for a viscoelastic homogeneous medium in the quasistatic case.

After obtaining the solution $u^{(33)}$ of (25) with the indicated set of boundary conditions, we compute the average vertical displacement $u_{s,3}^{(33,T)}(\omega)$ suffered by the boundary Γ^T . Then, the volume change $\Delta V(\omega)$ can be approximated by $\Delta V(\omega) \approx Lu_{s,3}^{(33,T)}(\omega)$, enabling us to compute $p_{33}(\omega)$ from (37).

4.2. Determination of p_{11} . Here we solve (25) in Ω with the fracture boundary conditions (5), (8), (9), (20), (22), and (23) together with the boundary conditions

$$(38) \quad \tau(\mathbf{u})\nu \cdot \nu = -\Delta P, \quad (x_1, x_3) \in \Gamma^R,$$

$$(39) \quad \tau(\mathbf{u})\nu \cdot \chi = 0, \quad (x_1, x_3) \in \Gamma,$$

$$(40) \quad \mathbf{u}_s \cdot \nu = 0, \quad (x_1, x_3) \in \Gamma \setminus \Gamma^R,$$

$$(41) \quad \mathbf{u}_f \cdot \nu = 0, \quad (x_1, x_3) \in \Gamma.$$

In this experiment $\epsilon_{33}(\mathbf{u}_s) = \epsilon_{22}(\mathbf{u}_s) = \nabla \cdot \mathbf{u}_f = 0$ and from (26) we see that this experiment determines p_{11} as indicated for p_{33} measuring the oscillatory volume change.

4.3. Determination of p_{55} . Consider the solution $u^{(55)}$ of (25) in Ω with the fracture boundary conditions (5), (8), (9), (20), (22), and (23) and the additional boundary conditions

$$(42) \quad -\boldsymbol{\tau}(\mathbf{u})\boldsymbol{\nu} = \mathbf{g}, \quad (x_1, x_3) \in \Gamma^T \cup \Gamma^L \cup \Gamma^R,$$

$$(43) \quad \mathbf{u}_s = 0, \quad (x_1, x_3) \in \Gamma^B,$$

$$(44) \quad \mathbf{u}_f \cdot \boldsymbol{\nu} = 0, \quad (x_1, x_3) \in \Gamma,$$

where

$$\mathbf{g} = \begin{cases} (0, \Delta G), & (x_1, x_3) \in \Gamma^L, \\ (0, -\Delta G), & (x_1, x_3) \in \Gamma^R, \\ (-\Delta G, 0), & (x_1, x_3) \in \Gamma^T. \end{cases}$$

The change in shape of the rock sample allows us to obtain $p_{55}(\omega)$ by using the relation

$$(45) \quad \text{tg}(\beta\omega) = \frac{\Delta G}{p_{55}(\omega)},$$

where $\beta(\omega)$ is the departure angle between the original positions of the lateral boundaries and those after applying the shear stresses (see, for example, [23]). Equation (45) holds for this experiment in a viscoelastic homogeneous media in the quasistatic approximation.

After computing the average horizontal displacement $u_{s,1}^{55,T}(\omega)$ suffered by the boundary Γ^T the change in shape suffered by the sample can be approximated by $\text{tg}(\beta(\omega)) \approx u_{s,1}^{55,T}(\omega)/L$, which from (45) determines $p_{55}(\omega)$.

4.4. Determination of p_{13} . Here we solve (25) in Ω with the fracture boundary conditions (5), (8), (9), (20), (22), and (23) and the boundary conditions

$$(46) \quad \boldsymbol{\tau}(\mathbf{u})\boldsymbol{\nu} \cdot \boldsymbol{\nu} = -\Delta P, \quad (x_1, x_3) \in \Gamma^R \cup \Gamma^T,$$

$$(47) \quad \boldsymbol{\tau}(\mathbf{u})\boldsymbol{\nu} \cdot \boldsymbol{\chi} = 0, \quad (x_1, x_3) \in \Gamma,$$

$$(48) \quad \mathbf{u}_s \cdot \boldsymbol{\nu} = 0, \quad (x_1, x_3) \in \Gamma^L \cup \Gamma^B,$$

$$(49) \quad \mathbf{u}_f \cdot \boldsymbol{\nu} = 0, \quad (x_1, x_3) \in \Gamma.$$

Thus, in this experiment $\epsilon_{22}(\mathbf{u}_s) = \nabla \cdot \mathbf{u}_f = 0$, and from (26) and (28) we get

$$(50) \quad \begin{aligned} \sigma_{11} &= p_{11}\epsilon_{11} + p_{13}\epsilon_{33}, \\ \sigma_{33} &= p_{13}\epsilon_{11} + p_{33}\epsilon_{33}, \end{aligned}$$

where ϵ_{11} and ϵ_{33} are the (macroscale) strain components at Γ^L and Γ^T , respectively. Then from (50) and the fact that $\sigma_{11} = \sigma_{33} = -\Delta P$ (cf. (46)), we obtain $p_{13}(\omega)$ as

$$(51) \quad p_{13}(\omega) = \frac{p_{11}\epsilon_{11} - p_{33}\epsilon_{33}}{\epsilon_{11} - \epsilon_{33}}.$$

4.5. Determination of p_{66} . Let us consider the solution of (25) in Ω with the fracture boundary conditions (5), (8), (9), (20), (22), and (23) and the following boundary conditions:

$$(52) \quad -\boldsymbol{\tau}(\mathbf{u})\boldsymbol{\nu} = \mathbf{g}_2, \quad (x_1, x_2) \in \Gamma^B \cup \Gamma^R \cup \Gamma^T,$$

$$(53) \quad \mathbf{u}_s = 0, \quad (x_1, x_2) \in \Gamma^L,$$

$$(54) \quad \mathbf{u}_f \cdot \boldsymbol{\nu} = 0, \quad (x_1, x_2) \in \Gamma,$$

where

$$\mathbf{g}_2 = \begin{cases} (\Delta G, 0), & (x_1, x_2) \in \Gamma^B, \\ (-\Delta G, 0), & (x_1, x_2) \in \Gamma^T, \\ (0, -\Delta G), & (x_1, x_2) \in \Gamma^R. \end{cases}$$

Then, we proceed as indicated for $p_{55}(\omega)$.

The stiffnesses coefficients p_{IJ} allow us to calculate the wave velocities and quality factors of the effective TIV medium as explained in Appendix C.

Figure 2 shows a schematic representation of the five quasistatic experiments.

5. A variational formulation to solve the BVP associated with p_{33} . Let us first introduce some notation. For $X \subset \mathbb{R}^d$ with boundary ∂X , let $(\cdot, \cdot)_X$ and $\langle \cdot, \cdot \rangle_{\partial X}$ denote the complex $L^2(X)$ and $L^2(\partial X)$ inner products for scalar, vector, or matrix valued functions. Also, for $s \in \mathbb{R}$, $\|\cdot\|_{s,X}$ will denote the usual norm for the Sobolev space $H^s(X)$ [24]. In addition, if $X = \Omega$ or $X = \Gamma$, the subscript X may be omitted such that $(\cdot, \cdot) = (\cdot, \cdot)_\Omega$ or $\langle \cdot, \cdot \rangle = \langle \cdot, \cdot \rangle_\Gamma$.

Let us define the following closed subspace of $[L^2(\Omega)]^2$:

$$\mathcal{V}_{33}(\Omega) = \{\mathbf{v} \in [L^2(\Omega)]^2 : \mathbf{v}|_{R^{(l)}} \in [H^1(R^{(l)})]^2, \mathbf{v} \cdot \boldsymbol{\nu} = 0 \text{ on } \Gamma \setminus \Gamma^T\}.$$

Also, set

$$H_0(\text{div}; \cup_l R^{(l)}) = \{\mathbf{v} \in [L^2(\Omega)]^2 : \mathbf{v}|_{R^{(l)}} \in H(\text{div}, R^{(l)}), \mathbf{v} \cdot \boldsymbol{\nu} = 0 \text{ on } \Gamma\},$$

$$\begin{aligned} H_0^1(\text{div}; \cup_l R^{(l)}) \\ = \{\mathbf{v} \in [L^2(\Omega)]^2 : \mathbf{v}|_{R^{(l)}} \in [H^1(R^{(l)})]^2 : \nabla \cdot \mathbf{v} \in H^1(R^{(l)}), \mathbf{v} \cdot \boldsymbol{\nu} = 0 \text{ on } \Gamma\}. \end{aligned}$$

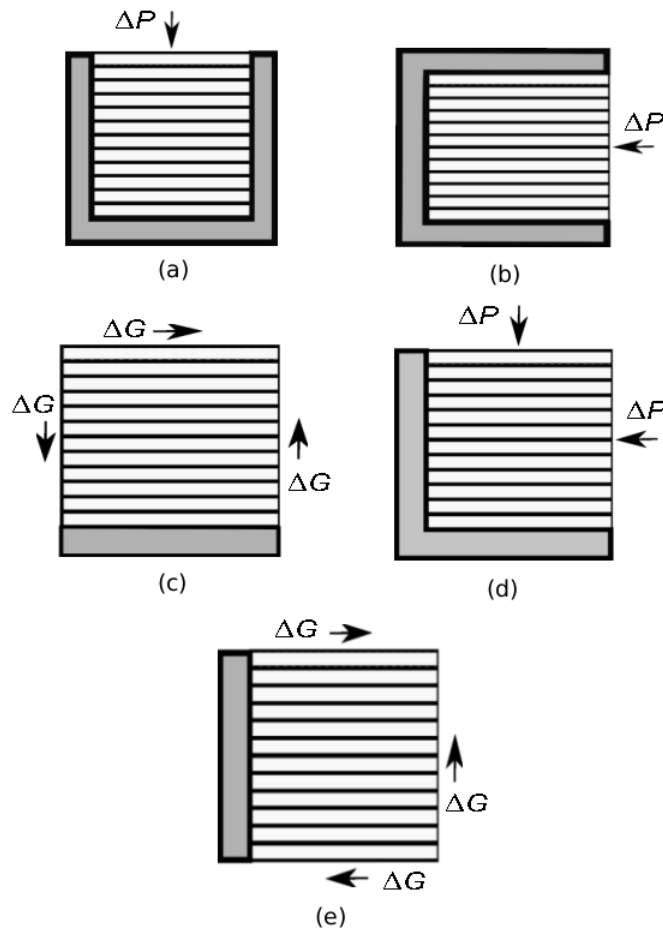


FIG. 2. Figures 1(a)–1(e) illustrate the five experiments needed to compute the stiffnesses components. In Figures 1(a) and 1(b) we show how to compute p_{33} and p_{11} using the boundary conditions (33)–(36) and (38)–(41), respectively. On the other hand, using the boundary conditions (42)–(44), we obtain the stiffness p_{55} by performing the experiment shown in 1(c) and the stiffness p_{66} with the experiment shown in 1(e) (boundary conditions (52)–(54)). Finally, Figure 1(d) displays the experiment to determine p_{13} using the boundary conditions (46)–(49).

Let

$$\mathcal{Z}_{33}(\Omega) = \mathcal{V}_{33}(\Omega) \times H_0(\text{div}; \cup_l R^{(l)}).$$

To obtain the variational formulation of the BVP associated with the determination of p_{33} as explained in section 4.1, multiply (25) by $\mathbf{v} = (\mathbf{v}_s, \mathbf{v}_f) \in \mathcal{Z}_{33}(\Omega)$, use integration by parts on each rectangle $R^{(l)}$ applying the fracture boundary conditions (5), (8), (9), (20), (22), and (23) and the additional boundary conditions (33), (34),

(35), and (36) to get *the weak form*: find $\mathbf{u}^{(33)} = (\mathbf{u}_s^{(33)}, \mathbf{u}_f^{(33)}) \in \mathcal{Z}_{33}(\Omega)$ such that

$$\begin{aligned} \Lambda(\mathbf{u}^{(33)}, \mathbf{v}) &\equiv i\omega \left(\frac{\mu^{(b)}}{\kappa^{(b)}} \mathbf{u}_f^{(33)}, \mathbf{v}_f \right) \\ &+ \sum_l \left(\tau_{st}(\mathbf{u}^{(33)}), \varepsilon_{st}(\mathbf{v}_s) \right)_{R^{(l)}} - \left(p_f(\mathbf{u}^{(33)}), \nabla \cdot \mathbf{v}_f \right)_{R^{(l)}} \\ &+ \sum_l \left\langle \mathbf{F} \left(\left[\mathbf{u}_s^{(33)} \cdot \boldsymbol{\nu}_{l,l+1} \right], \left[\mathbf{u}_s^{(33)} \cdot \boldsymbol{\chi}_{l,l+1} \right], \left[\mathbf{u}_f^{(33)} \cdot \boldsymbol{\nu}_{l,l+1} \right] \right)^T, \right. \\ &\quad \left. \left(\left[\mathbf{v}_s \cdot \boldsymbol{\nu}_{l,l+1} \right], \left[\mathbf{v}_s \cdot \boldsymbol{\chi}_{l,l+1} \right], \left[\mathbf{v}_f \cdot \boldsymbol{\nu}_{l,l+1} \right] \right)^T \right\rangle_{\Gamma^{(f,l)}} \\ &+ \sum_l \left\langle \frac{i\omega\mu^{(f)}\Pi}{\widehat{\kappa}^{(f)}} \frac{1}{4} \left(\mathbf{u}_f^{(33,l+1)} + \mathbf{u}_f^{(33,l)} \right) \cdot \boldsymbol{\nu}_{l,l+1}, \left(\mathbf{v}_f^{(l+1)} + \mathbf{v}_f^{(l)} \right) \cdot \boldsymbol{\nu}_{l,l+1} \right\rangle_{\Gamma^{(f,l)}} \\ (55) \quad &= - \langle \Delta P, \mathbf{v}_s \cdot \boldsymbol{\nu} \rangle_{\Gamma^T} \quad \forall \mathbf{v} = (\mathbf{v}_s, \mathbf{v}_f) \in \mathcal{Z}_{33}(\Omega). \end{aligned}$$

In (55) the superindex T indicates the transpose and the 3×3 complex matrix \mathbf{F} is given by

$$(56) \quad \mathbf{F} = \mathbf{F}_R + i\mathbf{F}_I = \begin{pmatrix} f_{11} & 0 & f_{12} \\ 0 & \frac{1}{\eta_T} & 0 \\ f_{12} & 0 & f_{22} \end{pmatrix},$$

where (see (19))

$$f_{11} = \frac{a_{22}}{\Theta} = f_{11,R} + if_{11,I}, \quad f_{12} = \frac{a_{12}}{\Theta} = f_{12,R} + if_{12,I}, \quad f_{22} = \frac{a_{11}}{\Theta} = f_{22,R} + if_{22,I}.$$

It will be assumed that \mathbf{F}_R is positive definite, that $f_{11,R} > 0$, and \mathbf{F}_I is nonnegative. These assumptions are valid for all physically meaningful data.

Note that in (55), we can write

$$(57) \quad \begin{aligned} &\sum_l \left(\tau_{st}(\mathbf{u}^{(33)}), \varepsilon_{st}(\mathbf{v}_s) \right)_{R^{(l)}} - \left(p_f(\mathbf{u}^{(33)}), \nabla \cdot \mathbf{v}_f \right)_{R^{(l)}} \\ &= \sum_{l=1}^{J(f)} \left(\mathbf{S}^{(b)} \tilde{\boldsymbol{\varepsilon}}(\mathbf{u}^{(33)}), \tilde{\boldsymbol{\varepsilon}}(\mathbf{v}) \right)_{R^{(l)}}. \end{aligned}$$

In (57), the matrix $\mathbf{S}^{(b)}$ and the column vector $\tilde{\boldsymbol{\varepsilon}}(\mathbf{u}^{(33)})$ are defined by

$$\mathbf{S}^{(b)} = \begin{pmatrix} \lambda_U^{(b)} + 2G^{(b)} & \lambda_U^{(b)} & \alpha^{(b)}M^{(b)} & 0 \\ \lambda_U^{(b)} & \lambda_U^{(b)} + 2G^{(b)} & \alpha^{(b)}M^{(b)} & 0 \\ \alpha^{(b)}M^{(b)} & \alpha^{(b)}M^{(b)} & M^{(b)} & 0 \\ 0 & 0 & 0 & 4G^{(b)} \end{pmatrix}, \quad \tilde{\boldsymbol{\varepsilon}}(\mathbf{u}^{(33)}) = \begin{pmatrix} \varepsilon_{11}(\mathbf{u}_s^{(33)}) \\ \varepsilon_{33}(\mathbf{u}_s^{(33)}) \\ \nabla \cdot \mathbf{u}_f^{(33)} \\ \varepsilon_{13}(\mathbf{u}_s^{(33)}) \end{pmatrix}.$$

Then we can state the variational formulation (55) in the equivalent form: find $\mathbf{u}^{(33)}$

$= (\mathbf{u}_s^{(33)}, \mathbf{u}_f^{(33)}) \in \mathcal{Z}_{33}(\Omega)$ such that

$$\begin{aligned}
 (58) \quad \Lambda(\mathbf{u}^{(33)}, \mathbf{v}) &\equiv i\omega \left(\frac{\mu^{(b)}}{\kappa^{(b)}} \mathbf{u}_f^{(33)}, \mathbf{v}_f \right) + \sum_l \left(\mathbf{S}^{(b)} \tilde{\boldsymbol{\varepsilon}}(\mathbf{u}^{(33)}), \tilde{\boldsymbol{\varepsilon}}(\mathbf{v}) \right)_{R^{(l)}} \\
 &+ \sum_l \left\langle \mathbf{F} \left(\left[\mathbf{u}_s^{(33)} \cdot \boldsymbol{\nu}_{l,l+1} \right], \left[\mathbf{u}_s^{(33)} \cdot \boldsymbol{\chi}_{l,l+1} \right], \left[u_f^{(33)} \cdot \boldsymbol{\nu}_{l,l+1} \right] \right)^T, \right. \\
 &\quad \left. \left(\left[\mathbf{v}_s \cdot \boldsymbol{\nu}_{l,l+1} \right], \left[\mathbf{v}_s \cdot \boldsymbol{\chi}_{l,l+1} \right], \left[v_f \cdot \boldsymbol{\nu}_{l,l+1} \right] \right)^T \right\rangle_{\Gamma^{(f,l)}} \\
 &+ \sum_l \left\langle \frac{i\omega\mu^{(f)}\Pi}{\widehat{\kappa}^{(f)}} \frac{1}{4} \left(\mathbf{u}_f^{(33,l+1)} + \mathbf{u}_f^{(33,l)} \right) \cdot \boldsymbol{\nu}_{l,l+1}, \left(\mathbf{v}_f^{(l+1)} + \mathbf{v}_f^{(l)} \right) \cdot \boldsymbol{\nu}_{l,l+1} \right\rangle_{\Gamma^{(f,l)}} \\
 &= - \langle \Delta P, \mathbf{v}_s \cdot \boldsymbol{\nu} \rangle_{\Gamma^T} \quad \forall \mathbf{v} = (\mathbf{v}_s, \mathbf{v}_f) \in \mathcal{Z}_{33}(\Omega).
 \end{aligned}$$

Problem (58) will be solved using a FEM to be described later, and the FE approximation to the solution $\mathbf{u}^{(33)}$ used as indicated in section 4.1.

5.1. Variational formulations for the solution of the BVP’s associated with p_{11}, p_{13}, p_{55} , and p_{66} . Let us define the spaces

$$\mathcal{V}_{11}(\Omega) = \{ \mathbf{v} \in [L^2(\Omega)]^2 : \mathbf{v}|_{R^{(l)}} \in [H^1(R^{(l)})]^2, \mathbf{v} \cdot \boldsymbol{\nu} = 0 \text{ on } \Gamma \setminus \Gamma^R \},$$

$$\mathcal{V}_{13}(\Omega) = \{ \mathbf{v} \in [L^2(\Omega)]^2 : \mathbf{v}|_{R^{(l)}} \in [H^1(R^{(l)})]^2, \mathbf{v} \cdot \boldsymbol{\nu} = 0 \text{ on } \Gamma^L \cup \Gamma^B \},$$

$$\mathcal{V}_{55}(\Omega) = \{ \mathbf{v} \in [L^2(\Omega)]^2 : v|_{R^{(l)}} \in [H^1(R^{(l)})]^2, \mathbf{v} = 0 \text{ on } \Gamma^B \},$$

$$\mathcal{V}_{66}(\Omega) = \{ \mathbf{v} \in [L^2(\Omega)]^2 : \mathbf{v}|_{R^{(l)}} \in [H^1(R^{(l)})]^2, \mathbf{v} = 0 \text{ on } \Gamma^L \}.$$

Next, for $(I, J) = (1, 1), (1, 3), (5, 5), (6, 6)$ let

$$\mathcal{Z}_{IJ}(\Omega) = \mathcal{V}_{IJ}(\Omega) \times H_0(\text{div}; \cup_l R^{(l)}).$$

A weak formulation for the BVP’s associated with the determination of p_{11}, p_{13}, p_{55} and p_{66} can be obtained applying the boundary conditions indicated in sections 4.2, 4.4, 4.3, and 4.5 and the fracture boundary conditions (5), (8), (9), (20), (22), and (23). Thus, we get the following problems:

- For p_{11} : find $\mathbf{u}^{(11)} = (\mathbf{u}_s^{(11)}, \mathbf{u}_f^{(11)}) \in \mathcal{Z}_{11}(\Omega)$ such that

$$(59) \quad \Lambda(\mathbf{u}^{(11)}, \mathbf{v}) = - \langle \Delta P, \mathbf{v}_s \cdot \boldsymbol{\nu} \rangle_{\Gamma^R} \quad \forall \mathbf{v} = (\mathbf{v}_s, \mathbf{v}_f) \in \mathcal{Z}_{11}(\Omega).$$

- For p_{13} : find $\mathbf{u}^{(13)} = (\mathbf{u}_s^{(13)}, \mathbf{u}_f^{(13)}) \in \mathcal{Z}_{13}(\Omega)$ such that

$$(60) \quad \Lambda(\mathbf{u}^{(13)}, \mathbf{v}) = - \langle \Delta P, \mathbf{v}_s \cdot \boldsymbol{\nu} \rangle_{\Gamma^R \cup \Gamma^T} \quad \forall \mathbf{v} = (\mathbf{v}_s, \mathbf{v}_f) \in \mathcal{Z}_{13}(\Omega).$$

- For p_{55} : find $\mathbf{u}^{(55)} = (\mathbf{u}_s^{(55)}, \mathbf{u}_f^{(55)}) \in \mathcal{Z}_{55}(\Omega)$ such that

$$(61) \quad \Lambda(\mathbf{u}^{(55)}, \mathbf{v}) = - \langle \mathbf{g}, \mathbf{v}_s \rangle_{\Gamma \setminus \Gamma^B} \quad \forall \mathbf{v} = (\mathbf{v}_s, \mathbf{v}_f) \in \mathcal{Z}_{55}(\Omega).$$

- For p_{66} : find $\mathbf{u}^{(66)} = (\mathbf{u}_s^{(66)}, \mathbf{u}_f^{(66)}) \in \mathcal{Z}_{66}(\Omega)$ such that

$$(62) \quad \Lambda(\mathbf{u}^{(66)}, \mathbf{v}) = - \langle \mathbf{g}_2, \mathbf{v}_s \rangle_{\Gamma \setminus \Gamma^L} \quad \forall \mathbf{v} = (\mathbf{v}_s, \mathbf{v}_f) \in \mathcal{Z}_{66}(\Omega).$$

Uniqueness for the solution of the variational problems is shown in the accompanying supplementary file (uniqueness.pdf [local/web 111KB]).

6. The FE method to solve the BVP's associated with the stiffnesses p_{IJ} . Let $\mathcal{T}^h(\Omega)$ be a nonoverlapping partition of Ω into rectangles Ω_j of diameter bounded by h such that $\bar{\Omega} = \cup_{j=1}^J \bar{\Omega}_j$. We will assume the Ω_j 's are such that their horizontal sides either have empty intersection or they coincide with one of the fractures. Let

$$(63) \quad \Omega^f = \cup_{j=1}^{I_f} \Omega_j, \quad \Omega^{Nf} = \Omega \setminus \Omega^f = \cup_{j=1}^{I_{Nf}} \Omega_j.$$

In (63) I_f is the number of Ω_j 's having one top or bottom side contained in some fracture $\Gamma^{(f,l)}$ for some l in the range $1 \leq l \leq J^{(f)}$, while I_{Nf} is the number of all Ω_j 's such that $\partial\Omega_j \cap \Gamma^{f,l} = \emptyset \ \forall l$.

Let

$$\mathcal{N}_j^h = P_{1,1}(\Omega_j) \times P_{1,1}(\Omega_j), \quad \mathcal{RTN}_j^h = P_{1,0}(\Omega_j) \times P_{0,1}(\Omega_j),$$

where $P_{s,t}(\Omega_j)$ denotes the polynomials of degree up to s in x_1 and up to t in x_3 on Ω_j . Denote by $\Gamma_{jk} = \partial\Omega_j \cap \partial\Omega_k$ the common side of two adjacent rectangles Ω_j and Ω_k and ν_{jk} the unit outer normal from Ω_j to Ω_k . Also, let $\Gamma_{jk}^{(f,l)} = \Gamma_{jk} \cap \Gamma^{(f,l)}$ and set

$$(64) \quad \mathcal{V}_{33}^{h,Nf}(\Omega^{Nf}) = \{ \mathbf{v}_s : \mathbf{v}_s|_{\Omega_j} \in \mathcal{N}_j^h, \mathbf{v}_s \text{ is continuous across } \Gamma_{jk} \ \forall \Omega_j \subset \Omega^{Nf}, \Omega_k \subset \Omega^{Nf}, \mathbf{v}_s \cdot \boldsymbol{\nu} = 0 \text{ on } \Gamma \setminus \Gamma^T \},$$

$$(65) \quad \mathcal{V}_{33}^{h,f}(\Omega^f) = \{ \mathbf{v}_s : \mathbf{v}_s|_{\Omega_j} \in \mathcal{N}_j^h \ \forall \Omega_j \subset \Omega^f, \mathbf{v}_s \text{ is continuous across } \Gamma_{jk} \text{ if } \Omega_k \subset \Omega^{Nf}, \mathbf{v}_s \cdot \boldsymbol{\nu} = 0 \text{ on } \Gamma \setminus \Gamma^T \}.$$

Also set

$$(66) \quad \mathcal{W}^{h,Nf}(\Omega^{Nf}) = \{ \mathbf{v}_f : \mathbf{v}_f|_{\Omega_j} \in \mathcal{RTN}_j^h, \mathbf{v}_f \cdot \boldsymbol{\nu}_{jk} \text{ is continuous across } \Gamma_{jk} \ \forall \Omega_j \subset \Omega^{Nf}, \Omega_k \subset \Omega^{Nf}, \mathbf{v}_f \cdot \boldsymbol{\nu} = 0 \text{ on } \Gamma \}$$

$$(67) \quad \mathcal{W}^{h,f}(\Omega^f) = \{ \mathbf{v}_f : \mathbf{v}_f|_{\Omega_j} \in \mathcal{RTN}_j^h \ \forall \Omega_j \subset \Omega^f, \mathbf{v}_f \cdot \boldsymbol{\nu}_{jk} \text{ is continuous across } \Gamma_{jk} \text{ if } \Omega_k \subset \Omega^{Nf}, \mathbf{v}_f \cdot \boldsymbol{\nu} = 0 \text{ on } \Gamma \}.$$

6.1. The FE method for the solution of the BVP associated with p_{33} .

To find a FE approximation $\mathbf{u}^{(h,33)}$ to $\mathbf{u}^{(33)}$ to be used to determine p_{33} we will employ the FE space

$$(68) \quad \mathcal{Z}_{33}^h(\Omega) = \left(\mathcal{V}_{33}^{h,Nf}(\Omega^{Nf}) \cup \mathcal{V}_{33}^{h,f}(\Omega^f) \right) \times \left(\mathcal{W}^{h,Nf}(\Omega^{Nf}) \cup \mathcal{W}^{h,f}(\Omega^f) \right).$$

The FE procedure associated to p_{33} is defined as follows: find $\mathbf{u}^{(h,33)} \in \mathcal{Z}_{33}^h(\Omega)$ such that

$$(69) \quad \Lambda(\mathbf{u}^{(h,33)}, \mathbf{v}) = - \langle \Delta P, \mathbf{v}_s \cdot \boldsymbol{\nu} \rangle_{\Gamma^T} \quad \forall \mathbf{v} \in \mathcal{Z}_{33}^h(\Omega).$$

6.2. The FE methods to solve the BVP's associated with p_{IJ} , $(I, J) =$

(1, 1), (1, 3), (5, 5), (6, 6). To formulate the FE procedures associated with determining p_{IJ} , $(I, J) = (1, 1), (1, 3), (5, 5), (6, 6)$, we define the $\mathcal{V}_{IJ}^{h,Nf}$ and $\mathcal{V}_{IJ}^{h,f}(\Omega^f)$ identically to the spaces $\mathcal{V}_3^{h,Nf}$ and $\mathcal{V}_{33}^{h,f}(\Omega^f)$ but changing the boundary conditions $\mathbf{v}_s \cdot \boldsymbol{\nu} = 0$ on $\Gamma \setminus \Gamma^T$ imposed in those spaces as follows:

- for $(I, J) = (1, 1)$ use $\mathbf{v}_s \cdot \boldsymbol{\nu} = 0$ on $\Gamma \setminus \Gamma^R$,
- for $(I, J) = (1, 3)$ use $\mathbf{v}_s \cdot \boldsymbol{\nu} = 0$ on $\Gamma^L \cup \Gamma^B$,
- for $(I, J) = (5, 5)$ use $\mathbf{v}_s = 0$ on Γ^B ,
- for $(I, J) = (6, 6)$ use $\mathbf{v}_s = 0$ on Γ^L .

Next, let

$$\mathcal{Z}_{IJ}^h(\Omega) = \left(\mathcal{V}_{IJ}^{h,N_f}(\Omega^{N_f}) \cup \mathcal{V}_{IJ}^{h,f}(\Omega^f) \right) \times \left(\mathcal{W}^{h,N_f}(\Omega^{N_f}) \cup \mathcal{W}^{h,f}(\Omega^f) \right).$$

Now, we formulate the FE procedures associated with determining the stiffnesses p_{IJ} 's as follows:

- $p_{11}(\omega)$: find $\mathbf{u}^{(h,11)} \in \mathcal{Z}_{11}^h(\Omega)$ such that

$$(70) \quad \Lambda(\mathbf{u}^{(h,11)}, \mathbf{v}) = - \langle \Delta P, \mathbf{v}_s \cdot \boldsymbol{\nu} \rangle_{\Gamma^R} \quad \forall \mathbf{v} \in \mathcal{Z}_{11}^h(\Omega).$$

- $p_{13}(\omega)$: find $\mathbf{u}^{(h,13)} \in \mathcal{Z}_{13}^h(\Omega)$ such that

$$(71) \quad \Lambda(\mathbf{u}^{(h,13)}, \mathbf{v}) = - \langle \Delta P, \mathbf{v}_s \cdot \boldsymbol{\nu} \rangle_{\Gamma^R \cup \Gamma^T} \quad \forall \mathbf{v} \in \mathcal{Z}_{13}^h(\Omega).$$

- $p_{55}(\omega)$: find $\mathbf{u}^{(h,55)} \in \mathcal{Z}_{55}^h(\Omega)$ such that

$$(72) \quad \Lambda(\mathbf{u}^{(h,55)}, \mathbf{v}) = - \langle \mathbf{g}, \mathbf{v}_s \rangle_{\Gamma \setminus \Gamma^B} \quad \forall \mathbf{v} \in \mathcal{Z}_{55}^h(\Omega).$$

- $p_{66}(\omega)$: find $\mathbf{u}^{(h,66)} \in \mathcal{Z}_{66}^h(\Omega)$ such that

$$(73) \quad \Lambda(\mathbf{u}^{(h,66)}, \mathbf{v}) = - \langle \mathbf{g}_2, \mathbf{v}_s \rangle_{\Gamma \setminus \Gamma^L} \quad \forall \mathbf{v} \in \mathcal{Z}_{66}^h(\Omega).$$

Uniqueness for the FE procedures (69)–(73) can be shown with the same argument used for the continuous case. Existence follows from finite dimensionality.

A set of a priori error estimates for the FE procedures to compute the solutions $u^{(h,IJ)}$, $(I, J) = (11), (33), (13), (55), (66)$ is included in Appendix A.

7. Numerical experiments. In this section we first validate the FE method to solve Biot's equations (69)–(73), which is the first step of the upscaling procedure presented.

Next, we validate the procedure to determine the stiffnesses p_{IJ} at the macroscale by comparison with the analytical solutions in [8] and summarized in Appendix B. For this purpose the corresponding energy velocities and dissipation coefficients are determined as indicated in Appendix C; see also [5].

Finally the complex stiffnesses $p_{IJ}(\omega)$, energy velocities, and dissipation coefficients are determined for the case of patchy brine-gas saturation for which no analytical solutions are available.

7.1. Validation of the FE method to solve the BVP's. Here we run experiments to check the validity of the solutions of the FE procedures (69)–(73) associated with the determination of the stiffnesses p_{IJ} . For this purpose we choose the variational formulation (71) to compute $\mathbf{u}^{(h,13)}$ for the case of nine fractures of fracture aperture 1 mm inside a square sample of side length 2 m and at a single frequency, chosen to be 30 Hz. Figure 3 shows a schematic representation of the configuration of the sample used in the validation procedure.

The material properties of background and fractures taken from [3] are given in Table 1. The saturant fluid is brine, with properties given in Table 2.

Since no analytical solution is available, we discretized the sample with a 960×960 uniform mesh and the computed solutions $\mathbf{u}^{(h,13)}$ for this fine mesh were taken as the reference solution to validate the FE solutions for other coarser meshes.

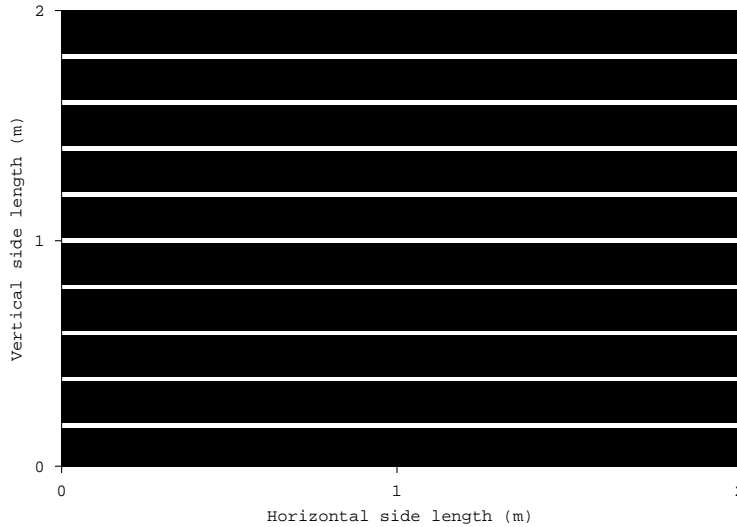


FIG. 3. Schematic representation of the sample Ω with nine fractures. Black regions correspond to the background and white regions correspond to fractures.

More specifically, the FE solution $u^{(h,13)}$ was computed for uniform meshes of mesh size $h = 0.0666, 0.0333, 0.0166, 0.0083$ meters ($30 \times 30, 60 \times 60, 120 \times 120$, and 240×240 uniform meshes), to obtain the numerical value of the exponent of h in the a priori error estimate given in Theorem A.1 in Appendix A.

The solution $\mathbf{u}^{(h,13)}$ for the fine mesh is referred to as $\mathbf{u}^{(ref)}$, while the solutions for the other four meshes are denoted as $\mathbf{u}^h, h = 0.0666, 0.0333, 0.0166, 0.0083$.

Let us define the following L^2 and broken $H^1(\Omega)$ plus $H(\text{div}, \Omega)$ errors of the FE procedure for each mesh size as

$$(74) \quad E_0^h = \|\mathbf{u}^{(ref)} - \mathbf{u}^h\|_0 = Ch^\alpha,$$

$$E_1^h = \sum_{l=1}^{J^{(f)}+1} \left(\|\mathbf{u}_s^{ref} - \mathbf{u}_s^{(h)}\|_{1,R^{(l)}} + \|\nabla \cdot (\mathbf{u}_f^{ref}) - \mathbf{u}_f^{(h)}\|_{0,R^{(l)}} \right) = Ch^\beta,$$

$$(75) \quad h = 0.0666, 0.0333, 0.0166, 0.0083.$$

In Table 3 we show the estimated values of the exponents α and β associated with the errors E_0^h and E_1^h defined in (74) and (75) for the four mesh sizes. This table shows the asymptotic convergence to the theoretical values 1 for the L^2 case and 0.5 for the broken $H^1(\Omega)$ plus $H(\text{div}, \Omega)$ case as given in Theorem A.1. These a priori error estimates are optimal due to the assumed regularity of the solution and the arguments given in Theorem A.1.

The solutions of the other variational problems yield similar results, which are omitted.

7.2. Validation of the quasistatic experiments to determine the stiffnesses p_{IJ} . In all the following experiments we used square samples of side length 2 m, with 9 fractures at equal distance of 20 cm and fracture aperture 1 mm.

The next experiment (Figures 4, 5, 6, 7, and 8) validates the FE procedure against the analytical solution given in [8] using a 50×50 mesh. Instead of showing graphs of the stiffness coefficients p_{IJ} , we show other physically meaningful quantities, i.e., the

TABLE 1
Material properties of background and fractures

Background	Solid grains bulk modulus, K_s	36. GPa
	solid grains density, ρ_s	2700 kg/m ³
	Dry bulk modulus K_m	9 GPa
	shear modulus G	7 GPa
	Porosity ϕ	0.15
	permeability κ	0.1 Darcy
Fractures	Solid grains bulk modulus, K_s	36. GPa
	solid grains density, ρ_s	2700 kg/m ³
	Dry bulk modulus K_m	0.0055 GPa
	shear modulus G	0.0033 GPa
	Porosity ϕ	0.5
	permeability κ	10 Darcy

TABLE 2
Fluid properties

Brine	bulk modulus, K_f	2.25 GPa
	density, ρ_f	1000 kg/m ³
	viscosity, μ	0.001 Pa · s
Gas	bulk modulus, K_f	0.012 GPa
	density, ρ_f	78 kg/m ³
	viscosity, μ	0.00015 Pa · s

energy velocities and dissipation coefficients for qP, qSV, and Sh waves, determined from the p_{IJ} 's as explained in Appendix C.

The material properties of background and fractures are the same as those in subsection 7.1 and given in Table 1. The saturant fluid is brine, with properties given in Table 2.

Figures 4, 5, 6, and 7 show polar plots of the energy velocity vector and dissipation factors $[(1000/Q)(\sin\theta, \cos\theta)]$ for qP, qSV waves as functions of the propagation angle, while Figure 8 displays a polar plot of the energy velocity vector for SH waves. Frequency is 30 Hz. Here 0 degrees and 90 degrees correspond to waves arriving parallel and normal to the fracture layering, respectively. A very good agreement between the numerical and analytical curves is obtained for all angles. The qP curves in Figures 4 and 5 show velocity anisotropy and strong attenuation for waves arriving normal to the fracture layering. On the other hand, Figures 6 and 7 show that qSV waves have stronger velocity anisotropy than qP waves, have no loss along the directions parallel and normal to the fracture layering, and have maximum attenuation at about 45 degrees. The energy velocity of qSV waves has the typical cuspidal triangles (or triplications), observed previously in fractured media [25]. Figure 8 shows that SH waves have velocity anisotropy; they are lossless.

Note that in the chosen frequency of 30 Hz the diffusive slow wave and its associated wave-induced fluid flow is properly being captured, matching the mesoscopic attenuation and dispersion effects predicted in the theory in [8].

7.3. Application of the quasistatic experiment to determine the stiffnesses p_{IJ} in the case of patchy brine-gas saturation. The last experiment considers the same sample but for full brine saturation, full gas saturation and 10% and 50% patchy brine-gas saturation. Brine and gas has the properties given in Table

TABLE 3
 Error analysis for the FE method to determine $\mathbf{u}^{(h,13)}$ using (71). Frequency is 30 Hz.

Mesh size h (m)	α	β
0.0666	0.48980	0.25411
0.0333	0.52559	0.27343
0.0166	0.66619	0.36171
0.0083	1.01407	0.51910

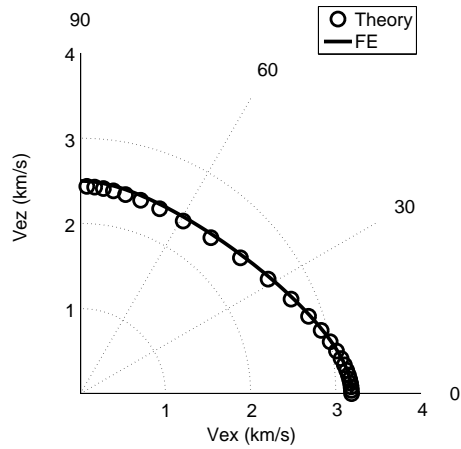


FIG. 4. Polar representation of the energy velocity of qP waves as function of the propagation angle. Frequency is 30 Hz. The symbols correspond to the FE experiments, while solid lines indicate the analytical values.

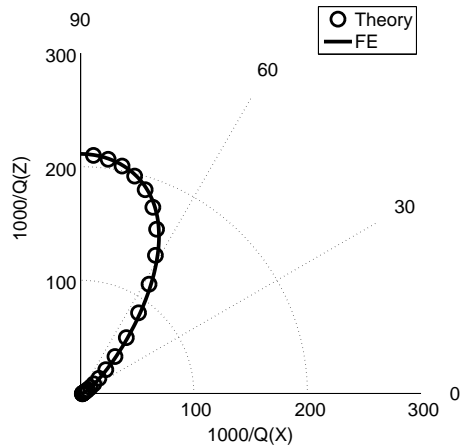


FIG. 5. Polar representation of the dissipation factor $[(1000/Q)(\sin\theta, \cos\theta)]$ of qP waves as a function of the propagation angle. Frequency is 30 Hz. Symbols correspond to the FE experiments, while solid lines indicate the analytical values.

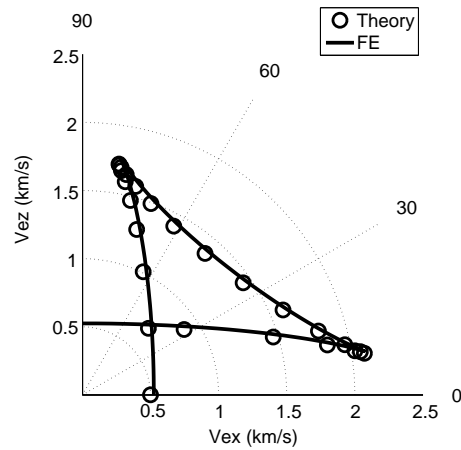


FIG. 6. Polar representation of the energy velocity of qSV waves as a function of the propagation angle. Frequency is 30 Hz. The symbols correspond to the FE experiments, while solid lines indicate the analytical values.

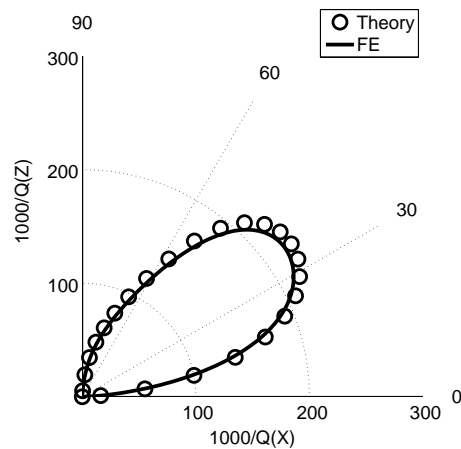


FIG. 7. Polar representation of the dissipation factor $[(1000/Q)(\sin\theta, \cos\theta)]$ of qSV waves as a function of the propagation angle. Frequency is 30 Hz. Symbols correspond to the FE experiments, while solid lines indicate the analytical values.

2. Frequency is 30 Hz and a 100×100 mesh was employed. No analytical solutions are available for the case of patchy brine-gas saturation, as it is the case for any heterogeneous fluid saturated fractured porous media.

Considering patchy distribution of fluids is relevant in practice since it may occur when shale strings seal off local pockets of gas, creating many gas-liquid contacts, or during hydrocarbon reservoir field production, when gas may come out of solution and create distributed pockets of free gas [6].

Patchy gas-brine distributions were generated using the procedure explained in

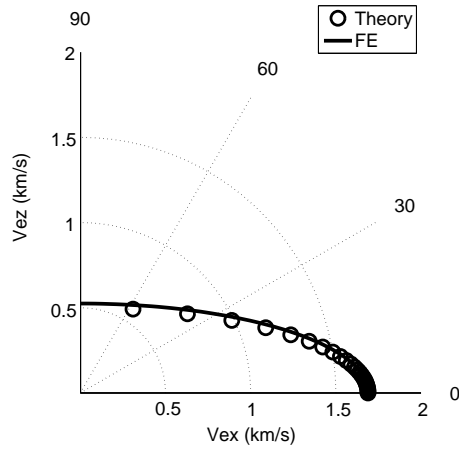


FIG. 8. Polar representation of the energy velocity of SH waves as a function of the propagation angle. Frequency is 30 Hz. The symbols correspond to the FE experiments, while solid lines indicate the analytical values.

[12], summarized below for completeness. To generate a patchy gas-brine saturation we employ the von Karman self-similar correlation function, which the spectral density is given by [26]

$$(76) \quad S_d(r_x, r_z) = N_0(1 + R^2 a^2)^{-(H+E/2)}.$$

Here, $R = \sqrt{r_x^2 + r_z^2}$ is the radial wavenumber, a the correlation length, H is a self-similarity coefficient ($0 < H < 1$), N_0 is a normalization constant, and E is the Euclidean dimension. The von Karman correlation (76) describes a self-affine, fractal processes of fractal dimension $D = E + 1 - H$ at a scale smaller than a . We choose $E = 2$, $D = 2.2$, and a to be 1.0% of the domain size. Once a continuous fractal distribution of brine is obtained over the 100×100 mesh and a threshold value S_b^* is selected, at each computational cell with brine saturation below and above S_b^* we assign either full gas or full brine saturation, respectively. Following this procedure two different patchy gas-brine distributions of overall 10% and 50% gas saturations were generated.

Figures 9, 10, 11, and 12 display polar plots of energy velocity vectors and quality of qP and qSV waves as a function of the propagation angle for 0%, 10%, 50%, and 100% global gas saturations. Frequency is 30 Hz. Figure 9 indicates that the velocity of qP waves decreases as gas saturation increases, while Figure 10 shows that qP anisotropy is enhanced by patchy saturation, is maximum for qP waves arriving normally to the fracture layering, and decreases as gas saturation increases. Maximum attenuation occurs at 10% gas saturation for all angles.

For qSV waves, Figure 11 shows that velocity decreases as gas saturation increases, with different anisotropic behavior depending on the value of gas saturation. Concerning the dissipation factor for qSV waves, Figure 12 shows maximum attenuation at 10% gas saturation, and decreasing anisotropy as gas saturation increases. Besides, qSV anisotropy shows different behavior for different values of gas saturation. The patchy nature of the saturation breaks the symmetry of the curves (see the

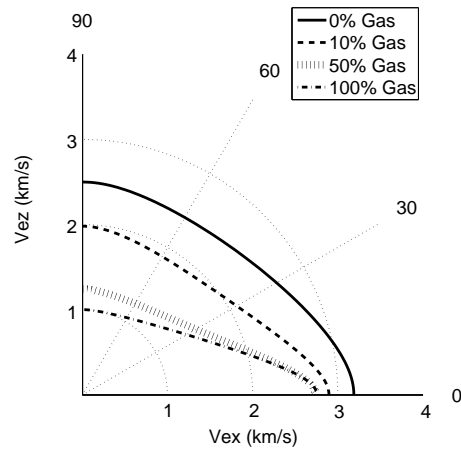


FIG. 9. Polar representation of the energy velocity of qP waves as a function of the propagation angle for full brine, full gas, and 10% and 50% patchy gas-brine saturation. The material properties of background and fractures are given in Table 1, while the saturant fluids are brine and gas with properties in Table 2. Frequency is 30 Hz.

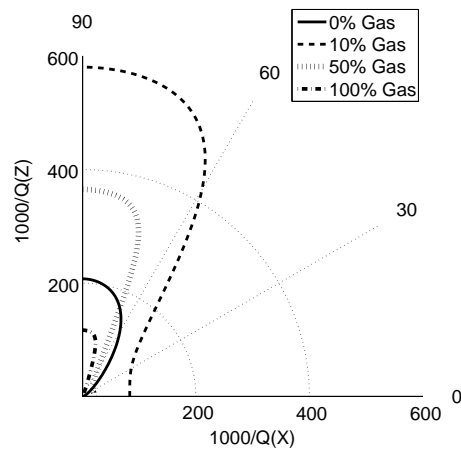


FIG. 10. Polar representation of the dissipation factor $[(1000/Q)(\sin\theta, \cos\theta)]$ of qP waves as a function of the propagation angle for full brine, full gas, and 10% and 50% patchy gas-brine saturation. The material properties of background and fractures are given in Table 1, while the saturant fluids are brine and gas with properties in Table 2. Frequency is 30 Hz.

cuspidal triangles in Figure 11), with the attenuation of the qSV wave having higher values at different angles.

On the other hand, the horizontally polarized shear (SH) wave is lossless and energy velocity of SH waves is unaffected by different values of gas saturation, the corresponding curves coincide with that in Figure 8 and are omitted.

Figure 13 shows the fluid pressure distribution (in Pa) for compressions normal

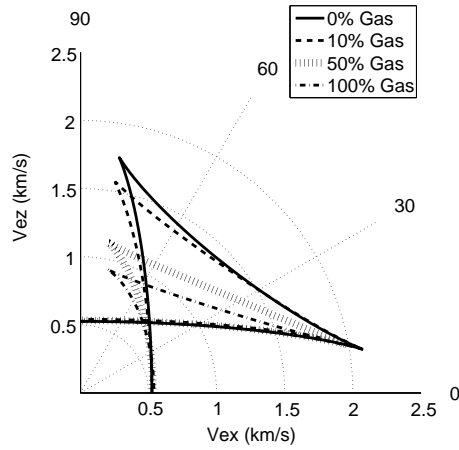


FIG. 11. Polar representation of the energy velocity of qSV waves as a function of the propagation angle for full brine, full gas, and 10% and 50% patchy gas-brine saturation. The material properties of background and fractures are given in Table 1, while the saturant fluids are brine and gas with properties in Table 2. Frequency is 30 Hz.

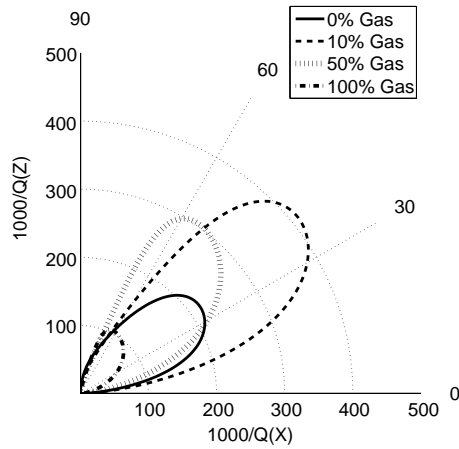


FIG. 12. Polar representation of the dissipation factor $[(1000/Q)(\sin\theta, \cos\theta)]$ of qSV waves as a function of the propagation angle for full brine, full gas, and 10% and 50% patchy gas-brine saturation. The material properties of background and fractures are given in Table 1, while the saturant fluids are brine and gas with properties in Table 2. Frequency is 30 Hz.

to the fracture layering (p_{33} experiment) for 10% patchy gas saturation, where the higher pressure values occur at the fracture locations, while the darker region values identify the gas patches. This figure illustrates the mesoscopic attenuation mechanism affecting compressional and shear waves at the macroscale and characterized in the previous patchy-related figures.

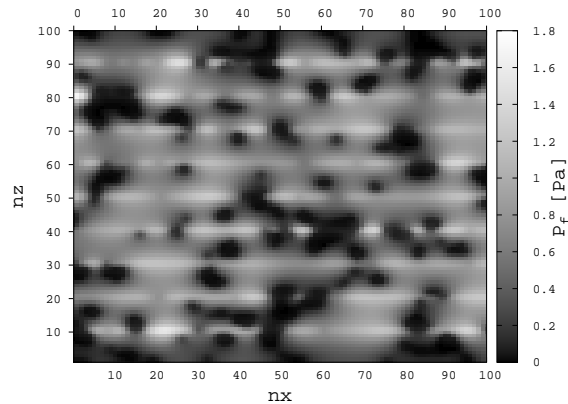


FIG. 13. Fluid pressure for normal compression to the fracture plane at 10% patchy gas-brine saturation. The material properties of background and fractures are given in Table 1, while the saturant fluids are brine and gas with properties in Table 2. Frequency is 30 Hz.

8. Conclusions. This work presented a FE procedure to determine the five complex and frequency-dependent stiffnesses of the TIV medium equivalent to a horizontally fractured Biot medium, with fractures represented as internal boundary conditions. These stiffnesses were determined by solving a collection of boundary value problems associated with compressibility and shear experiments formulated in the space-frequency domain, which were solved using the finite element method. A priori L^2 and H^1 error estimates were derived, which are optimal for the regularity of the solution; they were computationally confirmed carrying out mesh refinements.

The procedure was validated against analytical solutions, and then applied to arbitrarily heterogeneous fractured media, for which no analytical solutions are available. In particular, it was analyzed in the case of patchy gas-brine saturation.

The experiments show that fractures induce strong velocity and attenuation anisotropy, enhanced for the case of patchy saturation.

It is also shown that higher fluid pressure gradients occur close to the fractures, which illustrates the mesoscopic loss mechanism and in turn explains the strong velocity and attenuation anisotropy observed in fractured Biot media.

The procedure allows us to compute the complex stiffness components of the medium and the wave velocities and quality factors as a function of frequency and propagation angle. This is useful to obtain solutions for arbitrarily complex media when there is no analytical solution. Its applications range from oil exploration (reservoir rocks) to material science (artificial composite materials).

This study reveals that higher fluid pressure gradients occur close to the fractures and explains the strong velocity and attenuation anisotropy induced by fractures in Biot media.

Appendix A. A priori error estimates. The a priori error estimates are stated in the following theorem.

THEOREM A.1. Assume that for $(I, J) = (1, 1), (3, 3), (1, 3), (5, 5), (6, 6)$ $\mathbf{u}_s^{(IJ)} \in [H^{3/2}(\cup_l R^{(l)})]^2$ we have that $\mathbf{u}_f^{(IJ)} \in H_0^1(\text{div}; \cup_l R^{(l)})$. Also assume that \mathbf{F}_R is positive definite, that $f_{11,R} > 0$, and that \mathbf{F}_I is nonnegative. Then for sufficiently small $h > 0$ the following error estimate holds:

$$\begin{aligned}
 (77) \quad & \|\mathbf{u}^{(IJ)} - \mathbf{u}^{(h,IJ)}\|_0 \\
 & + h^{1/2} \left[\sum_{l=1}^{J^{(f)}+1} \left(\|\mathbf{u}_s^{(IJ)} - \mathbf{u}_s^{(h,IJ)}\|_{1,R^{(l)}} + \|\nabla \cdot (\mathbf{u}_f^{(IJ)} - \mathbf{u}_f^{(h,IJ)})\|_{0,R^{(l)}} \right) \right. \\
 & + \sum_{l=1}^{J^{(f)}} \sum_{jk} \left(\left\| \left[(\mathbf{u}_s^{(IJ)} - \mathbf{u}_s^{(h,IJ)}) \cdot \boldsymbol{\nu}_{l,l+1} \right] \right\|_{0,\Gamma_{jk}^{(f,l)}} \right. \\
 & + \left. \left\| \left[(\mathbf{u}_s^{(IJ)} - \mathbf{u}_s^{(h,IJ)}) \cdot \boldsymbol{\chi}_{l,l+1} \right] \right\|_{0,\Gamma_{jk}^{(f,l)}} \right. \\
 & + \left. \left. \left\| \left[(\mathbf{u}_f^{(IJ)} - \mathbf{u}_f^{(h,IJ)}) \cdot \boldsymbol{\nu}_{l,l+1} \right] \right\|_{0,\Gamma_{jk}^{(f,l)}} + \left\| (\mathbf{u}_f^{(IJ)} - \mathbf{u}_f^{(h,IJ)}) \cdot \boldsymbol{\nu}_{l,l+1} \right\|_{0,\Gamma_{jk}^{(f,l)}} \right) \right] \\
 & \leq C h \sum_{l=1}^{J^{(f)}+1} \left(\|\mathbf{u}_s^{(IJ,l)}\|_{3/2,R^{(l)}} + \|\mathbf{u}_f^{(IJ,l)}\|_{1,R^{(l)}} + \|\nabla \cdot \mathbf{u}_f^{(IJ,l)}\|_{1,R^{(l)}} \right).
 \end{aligned}$$

Proof. The proof is given in the accompanying supplementary file (apriori-error-proof.pdf [local/web 144KB]).

Appendix B. Mesoscopic-flow attenuation theory for anisotropic poroelastic media. White’s mesoscopic attenuation theory of interlayer flow [6], [4] describes the equivalent viscoelastic medium of a stack of two thin alternating porous layers of thickness d_1 and d_2 , such that the period of the stratification is $d = d_1 + d_2$. The theory gives the complex and frequency dependent stiffness p_{33} . White’s model has been generalized in [8] by Krzikalla and Müller to anisotropic media, i.e., they have obtained the five stiffnesses of the equivalent TI medium, denoted by p_{IJ} . The stress-strain relations is given by (26)–(31) and

$$(78) \quad p_{IJ}(\omega) = c_{IJ} + \left(\frac{c_{IJ} - c_{IJ}^r}{c_{33} - c_{33}^r} \right) [p_{33}(\omega) - c_{33}],$$

where c_{IJ}^r and c_{IJ} are the relaxed and unrelaxed stiffnesses.

According to Gelinsky and Shapiro [7, eq. (14)], the quasistatic or relaxed effective

constants of a stack of poroelastic layers are

$$\begin{aligned}
 c_{66}^r &= B_1^* = \langle \mu \rangle, \\
 c_{11}^r - 2c_{66}^r &= c_{12}^r = B_2^* = 2 \left\langle \frac{\lambda_m \mu}{E_m} \right\rangle + \left\langle \frac{\lambda_m}{E_m} \right\rangle^2 \left\langle \frac{1}{E_m} \right\rangle^{-1} \\
 &\quad + \frac{B_6^{*2}}{B_8^*}, \\
 c_{13}^r &= B_3^* = \left\langle \frac{\lambda_m}{E_m} \right\rangle \left\langle \frac{1}{E_m} \right\rangle^{-1} + \frac{B_6^* B_7^*}{B_8^*}, \\
 c_{33}^r &= B_4^* = \left\langle \frac{1}{E_m} \right\rangle^{-1} + \frac{B_7^{*2}}{B_8^*} \\
 (79) \quad &= \left[\left\langle \frac{1}{E_m} \right\rangle - \left\langle \frac{\alpha}{E_m} \right\rangle^2 \left\langle \frac{E_G}{M E_m} \right\rangle^{-1} \right]^{-1}, \\
 c_{55}^r &= B_5^* = \langle \mu^{-1} \rangle^{-1}, \\
 B_6^* &= -B_8^* \left(2 \left\langle \frac{\alpha \mu}{E_m} \right\rangle + \left\langle \frac{\alpha}{E_m} \right\rangle \left\langle \frac{\lambda_m}{E_m} \right\rangle \left\langle \frac{1}{E_m} \right\rangle^{-1} \right), \\
 B_7^* &= -B_8^* \left\langle \frac{\alpha}{E_m} \right\rangle \left\langle \frac{1}{E_m} \right\rangle^{-1}, \\
 B_8^* &= \left[\left\langle \frac{1}{M} \right\rangle + \left\langle \frac{\alpha^2}{E_m} \right\rangle - \left\langle \frac{\alpha}{E_m} \right\rangle^2 \left\langle \frac{1}{E_m} \right\rangle^{-1} \right]^{-1},
 \end{aligned}$$

where (with K_m, G, M, κ, μ) corresponding to the background in our notation (superindex $\theta = b$),

$$(80) \quad \lambda_m = K_m - \frac{2}{3}G \quad \text{and} \quad E_m = K_m + \frac{4}{3}G,$$

and we have also reported the notation of that paper for clarity. In the case of no interlayer flow, i.e., the unrelaxed regime, the stiffnesses are

$$\begin{aligned}
 c_{66} &= c_{66}^r, \\
 c_{11} - 2c_{66} &= c_{12} = 2 \left\langle \frac{(E_G - 2\mu)\mu}{E_G} \right\rangle + \left\langle \frac{E_G - 2\mu}{E_G} \right\rangle^2 \left\langle \frac{1}{E_G} \right\rangle^{-1}, \\
 (81) \quad c_{13} &= \left\langle \frac{E_G - 2\mu}{E_G} \right\rangle \left\langle \frac{1}{E_G} \right\rangle^{-1}, \\
 c_{33} &= \left\langle \frac{1}{E_G} \right\rangle^{-1}, \quad c_{55} = c_{55}^r,
 \end{aligned}$$

[7, eq. (15)], where

$$(82) \quad E_G = E_m + \alpha^2 M,$$

and M is given in (3).

Finally, the P-wave modulus p_{33} is [6] (also see in [5]),

$$(83) \quad p_{33} = \left[\frac{1}{c_{33}} + \frac{2(r_2 - r_1)^2}{i\omega(d_1 + d_2)(I_1 + I_2)} \right]^{-1},$$

where for each single layer

$$(84) \quad r = \frac{\alpha M}{E_G}, \quad I = \frac{\eta}{\kappa a} \coth\left(\frac{ad}{2}\right), \quad a = \sqrt{\frac{i\omega\mu E_G}{\kappa M E_m}}.$$

The main assumption in [8] is that the fluid-flow direction is perpendicular to the fracture layering and that the relaxation behavior is described by a single relaxation function or stiffness, i.e., $p_{33}(\omega)$. Thus the theory is valid for plane layers and cannot be used when 2D or 3D heterogeneities are present.

Appendix C. Wave velocities and quality factors. We consider homogeneous viscoelastic waves [5]. The complex velocities are the key quantity to obtain the wave velocities and quality factor of the equivalent anisotropic medium. They are given by

$$(85) \quad \begin{aligned} v_{qP} &= (2\bar{\rho})^{-1/2} \sqrt{p_{11}l_1^2 + p_{33}l_3^2 + p_{55} + A}, \\ v_{qSV} &= (2\bar{\rho})^{-1/2} \sqrt{p_{11}l_1^2 + p_{33}l_3^2 + p_{55} - A}, \\ v_{SH} &= \bar{\rho}^{-1/2} \sqrt{p_{66}l_1^2 + p_{55}l_3^2}, \\ A &= \sqrt{[(p_{11} - p_{55})l_1^2 + (p_{55} - p_{33})l_3^2]^2 + 4[(p_{13} + p_{55})l_1l_3]^2}, \end{aligned}$$

where $\bar{\rho}$ is the average density, $l_1 = \sin \theta$ and $l_3 = \cos \theta$ are the directions cosines, θ is the propagation angle between the wavenumber vector and the symmetry axis, and the three velocities correspond to the qP, qS, and SH waves, respectively. The phase velocity and quality factor are given by

$$(86) \quad v_p = \left[\operatorname{Re}\left(\frac{1}{v}\right) \right]^{-1}, \quad Q = \frac{\operatorname{Re}(v^2)}{\operatorname{Im}(v^2)},$$

where v represents either v_{qP} , v_{qSV} , or v_{SH} . The energy-velocity vector of the qP and qSV waves is given by

$$(87) \quad \frac{\mathbf{v}_e}{v_p} = (l_1 + l_3 \cot \psi)^{-1} \hat{\mathbf{e}}_1 + (l_1 \tan \psi + l_3)^{-1} \hat{\mathbf{e}}_3$$

in [5], where

$$(88) \quad \tan \psi = \frac{\operatorname{Re}(\beta^* X + \xi^* W)}{\operatorname{Re}(\beta^* W + \xi^* Z)}$$

defines the angle between the energy-velocity vector and the z -axis,

$$(89) \quad \beta = \sqrt{A \pm B}, \quad \xi = \pm \operatorname{pv} \sqrt{A \mp B}, \quad B = p_{11}l_1^2 - p_{33}l_3^2 + p_{55} \cos 2\theta,$$

where the upper and lower signs correspond to the qP and qS waves, respectively. Moreover,

$$(90) \quad W = p_{55}(\xi l_1 + \beta l_3), \quad X = \beta p_{11}l_1 + \xi p_{13}l_3, \quad Z = \beta p_{13}l_1 + \xi p_{33}l_3,$$

where “pv” denotes the principal value, which has to be chosen according to established criteria.

On the other hand, the energy velocity of the SH wave is

$$(91) \quad \mathbf{v}_e = \frac{1}{\rho v_p} (l_1 c_{66} \widehat{\mathbf{e}}_1 + l_3 c_{55} \widehat{\mathbf{e}}_3)$$

and

$$(92) \quad \tan \psi = \left(\frac{c_{66}}{c_{55}} \right) \tan \theta$$

[5, eq. 1.148], since p_{55} and p_{66} are real quantities.

In general, the phase velocity is related to the energy velocity by

$$(93) \quad v_p = v_e \cos(\psi - \theta),$$

where $v_e = |\mathbf{v}_e|$.

REFERENCES

- [1] B. GUREVICH, *Elastic properties of saturated porous rocks with aligned fractures*, J. Appl. Geophys., 54 (2003), pp. 203–218, <https://doi.org/10.1016/j.jappgeo.2002.11.002>.
- [2] B. GUREVICH, M. BRAJANOVSKI, R. J. GALVIN, T. M. MÜLLER, AND J. TOMS-STEWART, *P-wave dispersion and attenuation in fractured and porous reservoirs—poroelasticity approach*, Geophys. Prospect., 57 (2009), pp. 225–237, <https://doi.org/10.1111/j.1365-2478.2009.00785.x>.
- [3] S. NAKAGAWA AND M. A. SCHOENBERG, *Poroelastic modeling of seismic boundary conditions across a fracture*, J. Acoust. Soc. Am., 122 (2007), pp. 831–847, <https://doi.org/10.1121/1.2747206>.
- [4] J. M. CARCIONE AND S. PICOTTI, *P-wave seismic attenuation by slow-wave diffusion*, Effects of inhomogeneous rock properties, Geophysics, 71 (2006), pp. 01–08, <https://doi.org/10.1190/1.2194512>.
- [5] J. M. CARCIONE, *Wave Fields in Real Media. Theory and numerical simulation of wave propagation in anisotropic, anelastic, porous and electromagnetic media*, 3rd ed., extended and revised, Elsevier Science, Oxford, 2015.
- [6] J. E. WHITE, N. G. MIKHAYLOVA, AND F. M. LYAKHOVITSKIY, *Low-frequency seismic waves in fluid saturated layered rocks*, Phys. Solid Earth, 11 (1976), pp. 654–659.
- [7] S. GELINSKY AND S. A. SHAPIRO, *Poroelastic Backus-averaging for anisotropic, layered fluid and gas saturated sediments*, Geophysics, 62 (1997), pp. 1867–1878, <https://doi.org/10.1190/1.1444287>.
- [8] F. KRZIKALLA AND T. M. MÜLLER, *Anisotropic P-SV-wave dispersion and attenuation due to interlayer flow in thinly layered porous rocks*, Geophysics, 76 (2011), pp. WA135–WA145, <https://doi.org/10.1190/1.3555077>.
- [9] J. E. SANTOS, J. G. RUBINO, AND C. L. RAVAZZOLI, *A numerical upscaling procedure to estimate effective bulk and shear moduli in heterogeneous fluid-saturated porous media*, Comput. Methods Appl. Mech. Engrg., 198 (2009), pp. 2067–2077, <https://doi.org/10.1016/j.cma.2009.02.003>.
- [10] S. PICOTTI, J. M. CARCIONE, J. E. SANTOS, AND D. GEI, *Q-anisotropy in finely-layered media*, Geophys. Res. Lett., 37 (2010), L06302, <https://doi.org/10.1029/2009GL042046>.
- [11] J. E. SANTOS, S. PICOTTI AND J. M. CARCIONE, *Evaluation of the stiffness tensor of a fractured medium with harmonic experiments*, Comput. Methods Appl. Mech. Engrg., 247–248 (2012), pp. 130–145, <https://doi.org/10.1016/j.cma.2012.08.004>.
- [12] J. E. SANTOS AND J. M. CARCIONE, *Finite element harmonic experiments to model fractured induced anisotropy in poroelastic media*, Comput. Methods Appl. Mech. Engrg., 283 (2015), pp. 1189–1213, <https://doi.org/10.1016/j.cma.2014.08.016>.
- [13] E. H. SAENGER, R. CIZ, O. S. KRÜGER, S. M. SCHMALHOLZ, B. GUREVICH, AND S. A. SHAPIRO, *Finite-difference modeling of wave propagation on microscale: A snapshot of the work in progress*, Geophysics, 72 (2007), pp. SM293–SM300, <https://doi.org/10.1190/1.2753552>.
- [14] V. GRECHKA AND M. KACHANOV, *Effective elasticity of rocks with closely spaced and intersecting cracks*, Geophysics, 71 (2006), pp. D85–D91, <https://doi.org/10.1190/1.2197489>.
- [15] V. GRECHKA AND M. KACHANOV, *Effective elasticity of fractured rocks: A snapshot of the work in progress*, Geophysics, 71 (2006), pp. W45–W58, <https://doi.org/10.1190/1.2360212>.

- [16] P. A. RAVIART AND J. M. THOMAS, *A mixed finite element method for 2nd order elliptic problems*, in Proceedings of the Symposium on Mathematical Aspects of the Finite Element Method (Rome, 1975), Lecture Notes in Math. 606, Springer-Verlag, Berlin, 1977, pp. 292–315, <https://doi.org/10.1007/BFb0064470>.
- [17] M. A. BIOT, *Mechanics of deformation and acoustic propagation in porous media*, J. Appl. Phys., 33 (1962), pp. 1482–1498, <https://doi.org/10.1063/1.1728759>.
- [18] F. GASSMANN, *Über die elastizität poröser medien (On the elasticity of porous media)*, Vierteljahrsschrift der Naturforschenden Gessellschaft in Zurich, 96 (1951), pp. 1–23.
- [19] J. E. SANTOS, J. M. CORBERO, AND C. L. RAVAZZOLI, AND J. L. HENSLEY, *Reflection and transmission coefficients in fluid-saturated porous media*, J. Acoust. Soc. Am., 91 (1992), pp. 1911–1923.
- [20] M. A. BIOT, *Theory of propagation of elastic waves in a fluid-saturated porous solid. I. Low frequency range*, J. Acoust. Soc. Am., 28 (1956), pp. 168–178, <https://doi.org/10.1121/1.1908239>.
- [21] M. A. BIOT, *Theory of propagation of elastic waves in a fluid-saturated porous solid. II. High frequency range*, J. Acoust. Soc. Am., 28 (1956), pp. 179–191, <https://doi.org/10.1121/1.1908241>.
- [22] J. M. CARCIONE, *Anisotropic Q and velocity dispersion of finely layered media*, Geophys. Prosp., 40 (1992), pp. 761–783, <https://doi.org/10.1111/j.1365-2478.1992.tb00551.x>.
- [23] H. KOLSKY, *Stress Waves in Solids*, Clarendon Press, Oxford, 1953, [https://doi.org/10.1016/0022-5096\(54\)90045-9](https://doi.org/10.1016/0022-5096(54)90045-9).
- [24] R. A. ADAMS, *Sobolev Spaces*, Academic Press, New York, London, 1975.
- [25] J. M. CARCIONE, *Plane-layered models for the analysis of wave propagation in reservoir environments*, Geophys. Prosp., 44 (1996), pp. 3–26, <https://doi.org/10.1111/j.1365-2478.1996.tb00136.x>.
- [26] A. FRANKEL AND R. W. CLAYTON, *Finite difference simulation of seismic wave scattering: Implications for the propagation of short period seismic waves in the crust and models of crustal heterogeneity*, J. Geophys. Res., 91 (1986) pp. 6465–6489, <https://doi.org/10.1029/JB091iB06p06465>.